A Numerical Investigation of the Richtmyer-Meshkov Instability Using Front Tracking

A Dissertation Presented

by

Richard Lansing Holmes

to

The Graduate School
in Partial Fulfillment of the
Requirements
for the Degree of
Doctor of Philosophy

in

Applied Mathematics and Statistics

State University of New York
at Stony Brook

August 1994

Signature Page

Abstract of the Dissertation

A Numerical Investigation of the Richtmyer-Meshkov Instability Using Front Tracking

by

Richard Lansing Holmes

in

Applied Mathematics

State University of New York
at Stony Brook

1994

The method of front tracking is used to simulate the shock-tube experiments of Meshkov and Benjamin to predict perturbation amplitude growth rates. The results of the simulations are in much better agreement with experiment than previous simulations or theory. This improved agreement is explained by showing that simplifications in the theories, such as assumptions of incompressibility or linearity, miss crucial aspects of the experiments and

thus the theories give incorrect growth rates. In addition, it is shown that for simulations the correct time period for measurement of the instability is crucial in getting agreement with experiment.

The long-time behavior of the growth rates is discussed and the simulations are compared to an incompressible potential flow model for bubble velocities due to Hecht, et al. It is determined that the model adequately describes late-time behavior if modifications are made to take into account early time compressibility effects.

Finally, the simulations are validated through comparison with a linearized theory which is valid in the limit of small amplitudes.

Contents

List of Figures xi

List of Tables xii

Acknowledgements xiii

1 Introduction and Motivation 1

1.1 The Richtmyer-Meshkov Instability 2

1.2 Shock Tube Experiments 4

1.3 Measurements 6

1.4 Current Status 6

2 Previous Work 8

2.1 Theory 8

2.1.1 The Impulsive Model 9

2.1.2 Linear Theory 12

2.1.3 Fraley's Model 14

2.1.4 Potential Flow Model 14

2.1.5 Other Theories 15

2.2 Experiments 15
2.2.1 Meshkov 16
2.2.2 Benjamin 18
2.2.3 Zaytsev, Aleshin et al. 19
2.2.4 Related Experiments 19
2.3 Nonlinear Simulations 20
2.3.1 Meyer and Blewett 20
2.3.2 Cloutman and Wehner 21
2.3.3 Benjamin, Besnard and Haas 22
2.3.4 Other Experimental Simulations 23
2.3.5 Other Simulations 23

3 Front Tracking Method **24**

3.1 Tracked Waves 26
3.2 A Front Tracking Time Step 30
3.2.1 Front Propagation 30
3.2.2 Interior States 39
3.3 Achieving 2nd Order Accuracy 41
3.4 Diagnostics 43
3.5 Full vs. Partial Tracking 44
3.6 Parallelism 45

4 Simulation Results **47**

4.1 Computational Issues 47

4.1.1 Domain 47
4.1.2 Moving vs. Lab Frame 49
4.1.3 Artificial Viscosity 50
4.1.4 Full vs. Half-Wavelength 50
4.1.5 Artificial Surface Tension 51
4.2 Air-SF_6 Experimental Parameters 52
4.3 Air-SF_6 Perturbation Growth 53
4.4 Air-Helium Experimental Parameters 56
4.5 Air-Helium Perturbation Growth 57

5 Agreement with Experiment **61**
5.1 Role of Front Tracking 62
5.2 Role of Timing 64
5.3 Amplitude Disagreement 66
5.4 Translational Velocities 67

6 Asymptotic Behavior **70**
6.1 Decay 70
6.2 Bubble Velocity 72
6.3 Spike Velocity 75

7 Invalidity of Theories **77**
7.1 Simulation vs. Linear Theory 77
7.1.1 Air-SF_6 77
7.1.2 Air-Helium 84

7.2 Experiment vs. Linear Theory 86
7.3 Potential Flow Model 89
7.4 Fraley's Model 90
7.5 Improved Theories 91

8 Validation and Measurement Sensitivity 93
8.1 Comparison to Linear Theory 93
8.2 Mesh Refinement 98

9 Future Work and Conclusion 102
9.1 Future Work 102
9.2 Conclusion 103

Bibliography 105

List of Figures

1.1 Shock induced mixing in a supernova. Initial conditions. . . . 3

1.2 Shock induced mixing in supernova. Late time. 3

1.3 Schematic diagram of Richtmyer-Meshkov instability 5

2.1 Schematic diagram of Meshkovs shock tube 16

3.1 Pressure profiles of 1D shock waves in air using two shock-capturing methods and front tracking 25

3.2 Schematic representation of the grids used in front tracking . . 27

3.3 Triangulation of the computational domain in the region of a tracked wave 29

3.4 The normal and tangential vectors at a point to be propagated 31

3.5 Diagram showing estimate of new wave position and traceback of characteristics 33

3.6 The Riemann problems solved for the alternate point propagation routine 36

3.7 A refraction node propagation 40

4.1 The air-SF_6 interface at different times during the simulation . 54

4.2 Perturbation amplitude of the shocked air-SF_6 interface 55
4.3 Perturbation growth rate of the shocked air-SF_6 interface . . . 55
4.4 Air-helium interface at various times during the simulation . . 57
4.5 Perturbation amplitude of the shocked air-helium interface . . 58
4.6 Enlargement of the amplitude graph 58
4.7 Perturbation growth rate of the shocked air-helium interface . 59

5.1 Growth rate graph for air-SF_6 simulations with untracked and tracked incident shock 63
5.2 Amplitudes for air-SF_6 simulations with tracked and untracked incident shock waves 63
5.3 Contact translational velocity for the air-SF_6 simulation 68

6.1 Growth rate results of long time air-SF_6 simulation 71
6.2 Amplitude results of long time air-SF_6 simulation 71
6.3 Bubble velocities for long time air-SF_6 simulation 73
6.4 Log time vs. log velocity for bubble and spike velocities 73
6.5 Spike velocities for long time air-SF_6 simulations 76

7.1 Reproduction of the air-SF_6 growth rate graph 78
7.2 Pressure plots at a series of times for the nonlinear air-SF_6 solution 79
7.3 Simulation air-bubble and SF_6 spike velocities 80
7.4 Linear and nonlinear air-SF_6 solutions at $t = 195\mu$s 81
7.5 A test of the sinusoidal interface assumption of the linear theory for the air-SF_6 case. 84

7.6 A reproduction of the air-helium perturbation growth rate graph 85
7.7 Linear and nonlinear air-helium solutions at $t = 65\mu$s 87
7.8 A test of the sine shaped interface assumption for the air-helium case 88
7.9 Air-helium bubble velocity 88
7.10 Air-helium simulation spike velocity 89

8.1 The convergence of the nonlinear air-SF_6 simulations to the linearized solution 94
8.2 The convergence of the nonlinear air-helium simulations to the linearized solution 95
8.3 Normalized growth rates from air-SF_6 linear theory convergence tests. 97
8.4 Amplitudes from the air-SF_6 linear convergence test 97
8.5 Perturbation amplitude growth under mesh refinement for the air-helium simulations. 98
8.6 Mesh refinement studey for air-SF_6 99
8.7 mesh refinement tests for the air-SF_6 bubble velocity 100
8.8 Mesh refinement tests for the air-SF_6 spike velocity 100

List of Tables

4.1 Air-SF_6 Parameters 53

4.2 Air-Helium Parameters 56

Acknowledgements

I would like to thank my thesis advisor, Prof. John Grove, for his help, his guidance and his acceptance of my idiosyncrasies. This work would not have been possible without him. I would also like to thank Prof. James Glimm for his support and advice, and Dr. Yumin Yang for our many helpful discussions.

Finally, I would like to give my deepest thanks to my wife, RaeAnne, for her support and understanding over the last five years. I could not have done it without you.

Chapter 1

Introduction and Motivation

The behavior of shock-accelerated gas interfaces has received a great deal of attention due its fundamental importance in the study of various technological applications and natural phenomena. The basic phenomenon studied in this work is the Richtmyer-Meshkov instability. This instability is generated when a shock wave refracts through an interface separating two gases, causing perturbations on the interface to grow with time. It was originally predicted by Richtmyer [62] and subsequently observed in the experiments of Meshkov [54].

Presented here are the results of front tracking simulations of the Richtmyer-Meshkov instability. These simulations predict perturbation growth rates that are much closer to those in experiments than has previously been attained numerically or analytically. This improvement is due to the accuracy and stability of the front tracking method used in these computations as well as due to the proper consideration of nonlinear effects and measurement timing. The failure of the theories, which make assumptions about small amplitudes and/or incompressibility, is explained through an empirical analysis of nonlin-

ear, compressible waves. In addition, the asymptotic behavior of perturbation growth is studied and it is shown that a long term decay in the growth rate is to be expected and is part of the solution to the Euler equations, not a numerical artifact. Finally, the code is validated in a unique and convincing way by comparing the nonlinear simulations with reduced amplitudes with the solution of a linearized set of equations.

Preliminary accounts of this work can be found in [16, 17, 18, 19, 43, 45] and [47].

1.1 The Richtmyer-Meshkov Instability

Consider the situation shown in Figures 1.1 and 1.2. These figures show the initial and late-time configurations of a simulation of shock induced mixing in a supernova. In the first frame of Figure 1.1 we see the initial conditions. A circular shock wave is moving outward and will strike a perturbed circular material interface separating the heavy interior gas from the light outer gas. The second frame is an enlarged view of the initial conditions. Figure 1.2 shows the late time configuration. Instead of expanding in a circular fashion as may be expected given the nearly circular initial conditions, the initial perturbations have grown significantly and have forced heavy interior material deep into the surrounding light material. It is this growth of perturbations which constitutes the Richtmyer-Meshkov instability. This behavior has been suggested as one explanation for recent supernova observations in which x-rays from deep within the core of the exploding star are observed much earlier than

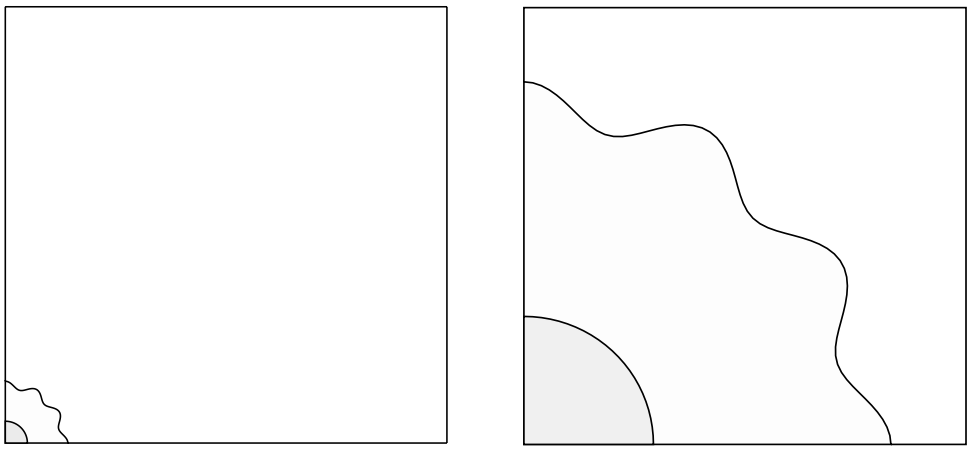

Figure 1.1: Results of simulation showing shock-wave induced mixing of gases. This type of mixing is thought to occur in supernovae. The initially small perturbations on the interface grow into large structures reaching deep into the surrounding material. This figure shows the initial configuration of the simulation.

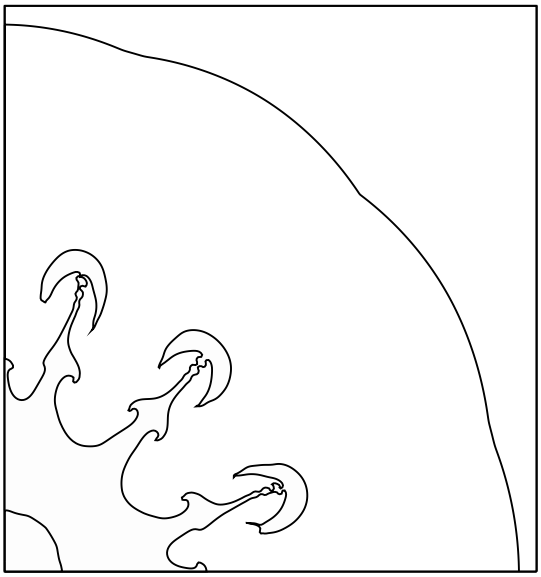

Figure 1.2: Late time behavior of the interface. The initially smooth interface perturbations have grown into large, complex structures reaching deep into the outer material. The outermost wave is the transmitted shock and the innermost wave is the trailing edge of the reflected rarefaction.

would be expected based on spherically symmetric models [2, 37, 59].

The Richtmyer-Meshkov instability also plays an important role in Inertial Confinement Fusion (ICF), a method proposed for generating usable energy from nuclear fusion [51, 68]. In ICF a small spherical fuel pellet made of a deuterium-tritium mix surrounded by a heavy shell is irradiated by a strong laser. The resulting explosive ablation generates a shock wave which compresses the pellet and, if the temperature and pressure are large enough, ignites a fusion reaction. The Richtmyer-Meshkov instability will limit the yield from this reaction since asymmetries will limit the amount of compression and will also force cold outer fuel into the central hot spot required for fusion.

1.2 Shock Tube Experiments

While many of the applications of Richtmyer-Meshkov instabilities involve circular geometries, most experiments have been performed in the rectangular geometry of a shock tube. Experiments in this geometry have the advantage of ease of setup and measurement, in addition to allowing simpler mathematical analysis. A diagram of such an experiment is given in Figure 1.3. The first frame shows a shock wave in a gas moving downward toward a material interface. We are viewing the interaction in a moving reference frame in which the mean position of the interface will be stationary after the passage of the shock. The interface is initially sinusoidal. In experiments this shape is imposed through the use of a thin (less than 1μm thick) membrane. In the second frame the shock is refracting through the interface, producing a

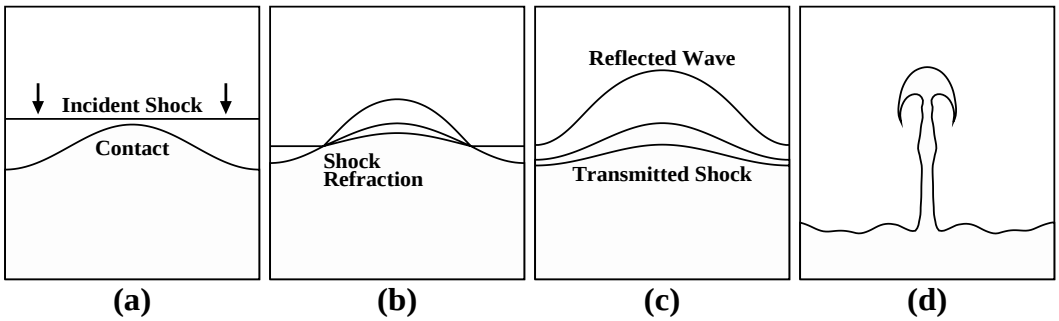

Figure 1.3: A schematic representation of the geometry of the Richtmyer-Meshkov instability. The interaction consists of the collision of a shock wave with a material interface. The refraction of the shock by the interface produces reflected and transmitted waves. The instability consists of the growth of perturbations of the material interface with time.

transmitted shock wave and a reflected wave which may be either a shock or rarefaction. The type of reflected wave that is produced depends on the thermodynamic properties of the two gases as well as the strength of the incident shock wave [32, 71]. By the third frame the shock has completed its refraction through the interface and both the transmitted and reflected waves are moving away from the interface. Due to shock compression the amplitude of the perturbation is smaller immediately after the interaction than it was originally. The amplitude will begin to increase again due to vorticity deposited on the interface by the refraction. The final frame shows the interface at late time. The initially smooth sinusoidal perturbation has grown into irregular "spikes" of the heavy fluid below reaching into the lighter material above and "bubbles" of the lighter material surrounding the spikes. We can see in this last picture the "mushroom caps" on the spikes that are characteristic of this instability. Note the width of the region of interpenetration has increased significantly.

1.3 Measurements

The primary quantity of interest in simulations and experiments of the Richtmyer-Meshkov instability is the width of the mixing layer as a function of time, i.e. the total amount of interpenetration of each material into the other. It is this quantity which determines the extent of heavy/light mixing in a supernova or which determines the effects of instabilities in an ICF pellet.

It is convenient to measure not the full width of the mixing layer but the perturbation amplitude, $a(t)$, defined as one-half of the vertical distance between the tips of the spikes and the tips of bubbles. This is exactly one-half of the mixing zone width. Also of interest is the perturbation amplitude growth rate $\dot{a}(t)$.

1.4 Current Status

Currently there is no satisfactory understanding of the Richtmyer-Meshkov instability. While the theoretical models agree well with each other and most numerical simulations agree with the theory, so far these fail to agree with most experimental results, predicting perturbation growth rates that are 40% to 200% larger than found in experiments. Due to the agreement of theory and computation it has generally been thought that the disagreement is due to experimental effects, specifically the effects of the membrane which initially separates the two experimental gases in shock tubes. Models of the membrane effect are not available, however, and this explanation has not been tested.

Theory and simulation have much to add in the study of the Richtmyer-

Meshkov instability. Theory gives us a deeper understanding than can be achieved through experiment alone, while simulation gives us the ability to make measurements that may be impractical or impossible to make in experiments and to perform on a computer more experiments than would be feasible to realize in a laboratory. It is very important to resolve the discrepancies between experiment, theory and simulation if we are to make significant progress in understanding the Richtmyer-Meshkov instability. We believe that this paper helps provide an improved understanding of this important and fundamental fluid interaction.

Chapter 2

Previous Work

There has been extensive work on the Richtmyer-Meshkov instability since the pioneering papers of Richtmyer [62] and Meshkov [54]. The literature can be divided into three areas: theory, experiment and simulation. Reviewed here is the literature relevant to the present work. See also the review by Rupert [63].

Of particular interest are the differences between the amplitude growth rates found by the theories, experiments and simulations, as well as whether each predicts a constant or a decaying growth rate.

2.1 Theory

There is currently no simple theory for Richtmyer-Meshkov instability growth rates which does not make assumptions of incompressibility, linear flow or potential flow. In Chapter 7 it is shown that all of these assumptions are violated in the experiments considered and it is primarily for this reason that there is disagreement between theories and experiment.

2.1.1 The Impulsive Model

The impulsive model, due to Richtmyer [62], is widely used to estimate instability growth rates due to its simplicity and its intuitive derivation. Richtmyer noted the similarities between the shock-induced instability and the Rayleigh-Taylor instability, which results when a heavy fluid is accelerated by a lighter one, and suggested that the shock-induced instability could be treated as a Rayleigh-Taylor instability with an impulsive acceleration. Indeed, as was later observed in shock tube experiments and simulations, the two instabilities are qualitatively similar in that they both have the same complex spike and bubble structures at late time (see Figure 1.3).

To derive Richtmyer's impulsive growth rate estimate we first consider the case of Rayleigh-Taylor instability between two incompressible fluids with an infinitesimal interface perturbation of the form $a(t)\cos(kx)$, where $a(t)k \ll 1$. Under these conditions a linearized equation for the perturbation amplitude as a function of time can be derived [26]:

$$\ddot{a} - kAga = 0 \tag{2.1}$$

$$a(t=0) = a_0 \tag{2.2}$$

$$\dot{a}(t=0) = 0 \tag{2.3}$$

where $A = (\rho_1 - \rho_0)/(\rho_1 + \rho_0)$ is the Atwood ratio and $g(t)$ is the gravitational acceleration pointing from the 1 fluid to the 0 fluid. This equation predicts stability for $A \leq 0$ and exponentially growing perturbations for $A > 0$.

Richtmyer proceeded by replacing the constant acceleration g by an im-

pulsive acceleration. That is, he set $g(t) = \Delta v \cdot \delta(t)$ in (2.1), where Δv is the change in interface velocity due to the action of the shock wave and $\delta(t)$ is the Dirac delta function. Making the substitution and integrating (2.1) gives an amplitude growth rate of

$$\dot{a}(t) = kA\Delta v a(0+) \tag{2.4}$$

where the post-shock amplitude, $a(0+)$, has been used in the integration and is given by

$$a(0+) = a(0-)(1 - \frac{\Delta v}{s}), \tag{2.5}$$

s being the incident shock speed. We interpret the subscripts 0 and 1 in the Atwood ratio calculation to denote the gases with the incident and transmitted shocks, respectively. Equation (2.4) is known as Richtmyer's impulsive model.

While the Rayleigh-Taylor instability has an exponential growth rate the impulsive model (2.4) predicts a constant growth rate for the Richtmyer-Meshkov instability. It is not clear, though, that this growth rate is realistic. There are several assumptions made: first, that the effects of a shock wave can be accurately modeled by an impulsive acceleration. Second, the derivation assumes that the effects of compressibility are negligible after the passage of the shock and, lastly, it assumes that the instability can be linearized.

Richtmyer originally considered only the case in which the shock refraction produced a reflected shock. As shown in [71], for polytropic gases a reflected rarefaction will result if the fluid parameters satisfy $\rho_0 c_0 > \rho_1 c_1$ and, as is the

case in all experiments considered here,

$$\frac{P_{behind} - P_{ahead}}{P_{ahead}} < 2\frac{\gamma_1\rho_1 - \gamma_0\rho_0}{(\gamma_0+1)\rho_0 - (\gamma_1+1)\rho_1}. \tag{2.6}$$

The relation between the acoustic impedances ρc implies that if

$$\frac{\gamma_0}{\gamma_1} > \frac{\rho_1}{\rho_0}. \tag{2.7}$$

then a reflected rarefaction will result. Since $\gamma_0/\gamma_1 \geq 3/5$ it is quite often the case that the inequality $\rho_1 < \rho_0$ implies a reflected rarefaction. Meyer and Blewett [56] used this fact to extend Richtmyer's impulsive model (2.4) to the reflected rarefaction case by allowing negative Atwood ratios.

According to (2.4) a negative Atwood ratio implies a negative growth rate. This can be interpreted as an inversion of the interface, which is indeed observed in experiments. For the case of a reflected rarefaction it is necessary in general to replace the post-shock amplitude in equation (2.4) by the average of the pre- and post- shock amplitudes in order to obtain agreement with simulations. This averaging process has no theoretical justification and is used only because it works better than other combinations.

Note that the discussion of reflected waves is based on the one dimensional theory and is only accurate for small initial amplitudes. Larger initial amplitudes can result in different behaviors.

Other work on the impulsive model includes its extension to circular and multilayer geometries by Mikaelian [57] and a discussion by Sturtevant [67] regarding possible ambiguities in the calculation of the post-shock amplitude, $a(0+)$.

2.1.2 Linear Theory

Recognizing the limitations in the derivation of the impulsive model, Richtmyer tackled the first two assumptions, the impulsive effects of the shock and incompressibility, by solving numerically a linearized system of compressible gas dynamics equations to calculate interface growth rates. The linear equations take into account compressibility effects, but they do not address the problem of finite amplitudes, i.e. we still have the requirement $a(t)k \ll 1$. Recently Yang, Zhang and Sharp [71] extended the linear theory of Richtmyer by including the case of a reflected rarefaction.

Briefly, derivation of the linearized system begins with the nonlinear Euler equations. Using the geometry described in Figure 1.3, a shock wave moving in the negative y-direction striking an unperturbed interface is taken to be the zero order solution. Small perturbations to the resulting Riemann solution are introduced and only first order quantities are kept. It is assumed that the interface perturbation is always sinusoidal and that all perturbed quantities q have the form $q(x, y, t) = q_0(y, t) + \delta q(y, t)e^{ikx}$, where $q_0(y, t)$ is the Riemann solution (and independent of x) and k is the wavenumber of the perturbation. If this solution ansatz is substituted into the Euler equations and terms of greater than first order in the δq's are ignored it can be shown that in each region bounded by the Riemann solution waves (contact, transmitted and reflected waves) the pressure perturbation $\delta P(y, t)$ satisfies the modified wave equation

$$\delta P_{tt} = c_0^2(\delta P_{yy} - k^2 \delta P) \tag{2.8}$$

where c_0 is the unperturbed sound speed in the region. For the reflected rarefaction case a set of three coupled PDE's is found for the region between the rarefaction edges.

In addition to the pressure equation (2.8) and the equations in the rarefaction fan, there are boundary conditions to consider. For the reflected shock case there are three boundaries: the transmitted shock, the reflected shock and the contact. For the reflected rarefaction case there are four since the reflected shock is replaced by the leading and trailing edges of the rarefaction. These boundary conditions are quite complicated and the reader is referred to the papers of Richtmyer [62] and Yang, et al. [71] for more details.

The solution of the linearized equations and boundary conditions generally predicts amplitude growth rates which begin at zero, rise quickly to a peak and subsequently perform decaying oscillations about a limiting value. Yang et al. [71] compared the predictions of the impulsive model (2.4) to the limiting results of the linearized theory, much as Richtmyer did but for a wider range of shock strengths and Atwood ratios. It was found that the impulsive model agrees well with the linearized predictions for weak shocks and Atwood ratios close to 1 and less well as the shock strength increases and/or the Atwood ratio goes to 0. This behavior is reasonable considering that the impulsive model assumes compressibility effects are negligible and this assumption will break down as the shock becomes stronger. In these comparisons the linearized predictions should be regarded as more accurate (in its domain of validity) than the impulsive model as it makes fewer approximating assumptions and

has a rigorous theoretical basis.

An interesting use of the linear theory is to validate the nonlinear front tracking simulations, using the fact that a correct nonlinear simulation should converge to the linear theory at early times as the initial perturbation amplitude decreases. Such a validation is performed in Chapter 8.

2.1.3 Fraley's Model

Fraley [36] has derived a model for the amplitude growth rate based on Laplace transforms of linearized Euler equations. As it results from a linearization, Fraley's model has the same region of validity as the linear theory of Richtmyer and Yang et al. His model has the advantage that it allows simplifications for very strong or very weak shocks.

Mikaelian found that for some fluid configurations Fraley's model is in better agreement with his simulations than the impulsive model. See [58]. The predictions of Fraley's model are compared to the front tracking simulations in Chapter 7.

2.1.4 Potential Flow Model

Hecht et al. [46] derived a model for the bubble velocity in the Rayleigh-Taylor instability which they extended to include the Richtmyer-Meshkov instability. Their model is unique in that it is intended to address multiple timescales in the instability, late time as well as the linear period, and all initial amplitudes.

This model is based on the assumption that the dynamics of the bubble can be adequately described by considering only the flow near the bubble tips.

They also assume that the flow is incompressible and irrotational in this region so that a velocity potential can be defined. They limit their analysis to the case $A \approx 1$. Their model gives the rather surprising prediction that the bubble reaches an asymptotic velocity of $2/(3kt)$ independent of the initial amplitude and shock strength. In Chapter 6 it is shown that this model does a good job predicting the asymptotic velocity of the bubble if early time compressibility effects are taken into account.

It should be stressed that this model addresses only the bubble velocity. In the applications discussed (supernovae, ICF) it is usually the spike behavior that is most important.

2.1.5 Other Theories

There are other theories of fluid instabilities that are related to the subject of this paper but not directly applicable. For the Rayleigh-Taylor instability see [26] and [65]. In [7, 12, 13, 14, 15] Bernstein and Book consider the stability of explosions and implosions while Goodman [41] considers the stability of self-similar expansions against convection.

2.2 Experiments

There are relatively few examples of Richtmyer-Meshkov instability experiments that use a sharp sinusoidal perturbation. Besides the early experiments of Meshkov there are more recent experiments by Benjamin and Zaytsev, Aleshin et al. We perform simulations of certain experiments of Meshkov

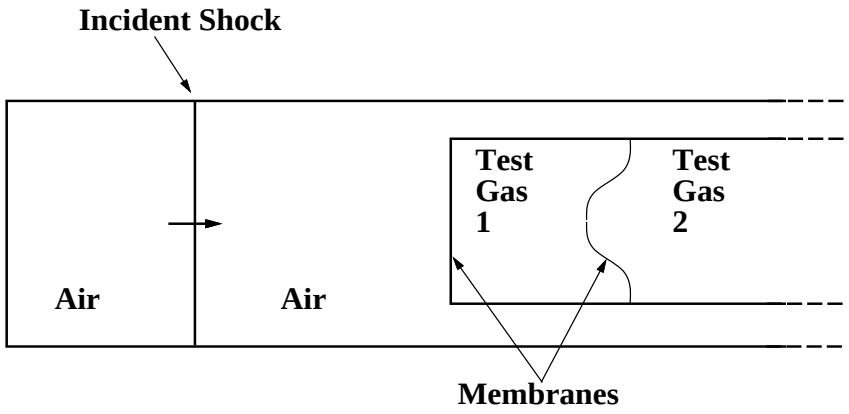

Figure 2.1: A schematic representation of Meshkov's experimental shock tube. A shock is generated in air which strikes the test section. This produces a shock in the first test gas which will strike the perturbed membrane and excite the instability.

and Benjamin.

2.2.1 Meshkov

In 1970 Meshkov reported on shock tube experiments testing the predictions of Richtmyer's impulsive and linear theories. He used several combinations of air, Freon-22, helium and carbon dioxide. The experimental setup consisted of a test section containing the two gases of interest separated by a thin nitrocellulose membrane approximately 1 micron thick. A small perturbation of wavelength 4cm and amplitude either 2mm or 4mm was imposed on the membrane. This test section was enclosed in a shock tube filled with air with another membrane on each end of the test section to enclose it. A Mach 1.52 shock in air was generated in the shock tube which struck the end of the test section and generated a shock there. This shock wave struck the interface and excited the instability. A schematic diagram is given in Figure 2.1.

Schlieren photographs of the test section allowed Meshkov to obtain a time history of the perturbation amplitude. His experiments showed the expected qualitative behavior, with the perturbation amplitude growing in time and, in the experiments with a reflected rarefaction, an interface phase inversion.

While the instability growth appeared to be linear in his experiments, the growth rates did not agree with those predicted by the impulsive model. In experiments with a shock in helium incident on an interface with air, for example, the impulsive model predicts a growth rate that is approximately three times too large. Similar discrepancies were reported for the other gas combinations as well. He attributes the difference to the fact that the experimental amplitude is beyond the small-amplitude linear regime, to diffusion during the experiment, and to possible impurity of the gases. It should be noted that his comparisons are made to the transformed impulsive model

$$\frac{d(a/a(0-))}{d(l/\lambda)} = 2\pi A \frac{a(0+)}{a(0-)} \tag{2.9}$$

where $l = \Delta v \cdot t$ is the distance traveled by the interface.

Meshkov solved the Riemann problem between the driving air shock and the incident test gas in order to find the incident shock strength and an estimate of the shock compressed interface amplitude, $a(0+)$, used in equation (2.9). It is important to do this calculation before comparing Meshkov's experiments to other theories or to simulations.

2.2.2 Benjamin

More recent experiments have been performed by Benjamin [4, 5, 6]. In his experiments Benjamin used two gas combinations: an air shock incident on an interface with sulfur hexafluoride (SF_6) and an air shock incident on an interface with helium. In both cases a thin (0.5 micron) membrane was used to separate the gases.

Benjamin's air-SF_6 and air-helium experiments showed the expected qualitative behavior, with an interface inversion for the air-helium experiments and growth of the perturbations with time. He reports a factor of 1.35 disagreement between the growth rates of the impulsive model and his SF_6 experiments. However, to find the amplitude of the compressed interface for use in (2.4) he extrapolates backward in time from his late time amplitudes and finds an initial shock-compressed amplitude that is approximately 35% smaller than predicted by (2.5). The use of this extrapolated amplitude is not well-established, especially in light of the agreement between the shock-compressed amplitudes given by (2.5) and the nonlinear front tracking simulations (see Chapters 4). Using the amplitude given by (2.5) Benjamin's experimental growth rates are a factor of two smaller than predicted by the impulsive model.

Similarly, in his air-helium experiments he finds a growth rate one-half the value predicted by the impulsive model using the average of the pre- and post-shock amplitudes in equation (2.4).

Benjamin finds, as did Meshkov, that the growth rate of the interface is fairly constant during the observation period. At the end of the single shock

experiments $ka \approx 1.4$, well past the time nonlinear effects are expected.

2.2.3 Zaytsev, Aleshin et al.

Zaytsev, Aleshin et al. [1, 72] conducted Richtmyer-Meshkov instability experiments using very strong incident shocks, approximately Mach 3.5, striking an argon-xenon interface. Their experimental growth rates agreed relatively well with the impulsive model. In addition, they saw a decay in the perturbation growth rate at late times when $ka \approx 3$.

There are several possible reasons why they achieve agreement with the impulsive model. First, they use a much stronger shock wave than either Meshkov or Benjamin (Mach 3.5 vs. 1.52 and 1.2, respectively) which should help negate strength and inertial effects of the membrane. In addition, they used a thicker membrane (2μm) which would reduce diffusion across the interface before shocking. It may also be significant that the monotonic gases used in these experiments have very similar equations of state.

2.2.4 Related Experiments

Some related experiments using continuous interfaces are those of Sturtevant and Brouilette [21], Bonazza [11] and Brouilette [20]. See also [35] for a report of Richtmyer-Meshkov experiments using the Nova laser. Budzinski [22] and Jacobs [48] report on experiments using shocked cylinders in air, Budzinski using helium cylinders and Jacobs using helium and SF_6. In [23] and [49] Budzinski et al. and Jacobs et al. present experiments using shocked SF_6 curtains.

2.3 Nonlinear Simulations

As mentioned above, Richtmyer [62] and Yang, et al. [71] report the results of linearized simulations of the Richtmyer-Meshkov instability. These linear simulations generally agree with the impulsive model in their predictions of amplitude growth rates. However, these predictions do not agree with the results of experiment. Since the linear simulations and the impulsive model ignore some of the nonlinear physical effects it is possible that these effects are significant in experiments and must be included in any model. One method to study these effects on the Richtmyer-Meshkov instability is to perform fully nonlinear compressible simulations of the Euler equations.

Previous simulations of Richtmyer-Meshkov experiments generally show a significant discrepancy between the simulated growth rates and the experimentally measured ones. Indeed, the fully nonlinear simulations have, so far, given results closer to the linear simulations than to the experiments. Since the simulations did not model strength or inertial effects of the membrane used in experiments, this is commonly cited as the reason for the discrepancy.

2.3.1 Meyer and Blewett

The first published results of nonlinear Richtmyer-Meshkov instability simulations are from Meyer and Blewett [56]. They use a Lagrangian code to simulate Meshkov's experiments. They report growth rates from an early-time period of linear growth and find that the simulated growth rate is very close to that predicted by the impulsive model (2.4). Thus their simulations give the same

factor of two increase in the growth rate relative to experiments as does the impulsive model. It is important to note that in the two simulations for which they give explicit amplitude vs. time data they do not run their simulations for the full experimental time and, in fact, end their simulations before Meshkov has taken any experimental data. It is be shown in Chapter 5 that measuring growth rates too early makes a dramatic difference in the results.

Note that in order to reach agreement with the impulsive model in the case of negative Atwood ratios Meyer and Blewett used the average of the pre- and post-shock amplitudes as the impulsive model initial amplitude (compare equation (2.5)).

2.3.2 Cloutman and Wehner

More recently Cloutman and Wehner [29] performed simulations of Benjamin's 1988 experiments [4] using an Eulerian code and a volume tracking interface algorithm. Their simulations show a much larger growth rate than experiment– again by a factor of two in both the air-SF_6 and air-helium simulations. They report only a single growth rate for each simulation so it is not clear whether they observe decay in the growth rate.

Cloutman and Wehner discuss additional simulations using a three-dimensional initial perturbation of the form $a_0 \cos(k_x x)\cos(k_y y)$ (for the two-dimensional experiments $k_y = 0$). The growth rates from these simulations are lower than those of the two dimensional simulations and closer to that found in experiment. An interesting aspect of the decrease in the growth rates is that a three dimensional extension of the impulsive model (2.4) would predict a growth

rate proportional to $\sqrt{k_x^2 + k_y^2}$. Thus the impulsive model indicates growth rates larger by a factor of $\sqrt{2}$ in three dimensions compared with three dimensions. This inconsistency with simulations may indicate that the linearized theories are not applicable, although there is the possibility that their three dimensional simulations were underresolved and predicted incorrect growth rates.

2.3.3 Benjamin, Besnard and Haas

In [6] Benjamin, Besnard and Haas report the results of their simulations using an Eulerian code with SLIC [60]. While their simulations are in good agreement with the impulsive model (2.4) at early times, they note a decay in the growth rate that at late times reduces the growth rate to experimental levels. Averaging the simulation growth rate over the experimental time period reduces the discrepancy with experiment to a level approximately 40% higher than the experimental average and approximately 20% higher than the front tracking simulations of the same experiment (see Chapter 4). They contend that the decay is numerical rather than physical. The decay is an important aspect of their computations (and of the front tracking simulations as well) and is considered in detail in Chapter 6.

They also report that the mean translational velocity of the air-SF_6 and air-helium interfaces is significantly larger than expected based on 1D theory or nonlinear simulation. They interpret this to be an indication of contamination of the experimental gases due to pre-shock diffusion across the membrane. This is considered in Chapter 5.

2.3.4 Other Experimental Simulations

In [9] the results of several numerical codes, including the front tracking method, are reported. Among the results presented are the simulated growth rates of Benjamin's 1988 air-helium experiment. All of these rates were much larger than experiment, again by a factor of two except for front tracking which was off by a factor of approximately 1.6. The large difference between the numerical results and the experimental results, as well as the striking agreement among the various numerical methods, led the authors of that paper to suspect the experimental membrane effects as part of the reason for the discrepancy.

2.3.5 Other Simulations

There are many other reports of Richtmyer-Meshkov instability simulations which do not address the agreement between codes and experiment. See, for example, [25, 52, 58, 61], and the volumes [8], [33] and [50].

Chapter 3

Front Tracking Method

Front Tracking is a numerical method for high resolution computations involving well defined waves. The basic idea of front tracking is to couple a standard numerical method on a rectangular grid with lower dimensional dynamic moving grids to follow the desired waves. It has been used successfully in simulations of compressible gas dynamics (present work as well as [24, 27, 38, 39]), oil and water reservoirs [34, 40] and elasto-plastic waves [70].

The main advantage of front tracking is that it eliminates the numerical diffusion that is inherent in any standard finite-difference method. By tracking discontinuous waves one can explicitly include jumps in the state variables across the waves and keep all discontinuities perfectly sharp. This is in contrast with finite difference codes that typically spread shocks over 3-4 computational zones and contact discontinuities over much larger regions. It is much less diffusive than interface reconstruction methods such as SLIC [60] which reduce but do not eliminate numerical diffusion.

The lack of numerical diffusion is most important in computing wave inter-

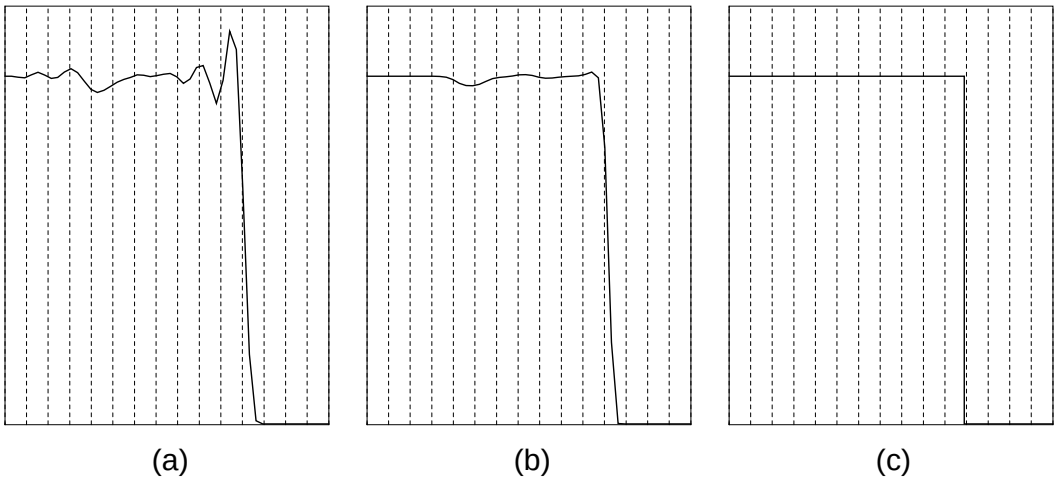

Figure 3.1: Pressure profiles of 1D shock waves in air using two shock-capturing methods and front tracking. a) Lax-Wendroff, b) MUSCL, c) Front tracking. Front tracking completely eliminates post-shock oscillation. In addition, behind the shock-captured waves we see a slight dip in pressure due to an entropy error at shock initiation. Front tracking is not susceptible to such errors.

actions. With front tracking one can resolve the shock-contact interactions in the Richtmyer-Meshkov instability at sub-grid level. In addition, Menikoff showed [53] that the artificially large shock transition regions of standard shock-capturing schemes can cause errors in the computation of wave interactions.

Another advantage of front tracking is that by tracking the discontinuities and applying special algorithms to them nonlinear instabilities and post-shock oscillations common to other methods are reduced (see Figure 3.1).

Front tracking also gives position and state information for measuring the growth of the unstable interfaces, which is quite useful for the Richtmyer-Meshkov instability computations presented here.

Details of the front tracking method have been given elsewhere [28, 44].

The following description concentrates on those aspects of the method which are most important for the success of the present computations.

3.1 Tracked Waves

Figure 3.2 shows the basic front tracking setup with a tracked wave embedded in a rectangular grid. A tracked wave, known as a *front* or *curve*, is a piecewise linear representation of a physical wave. Each linear segment of the curve is called a *bond* and the intersection of two bonds is known as a *point*. State variables are assigned on each side of a point to represent the limiting value of the interior states as we approach the point from either side. The two states represent the discontinuity across the wave. Since the discontinuity is sharp numerical diffusion is eliminated. An orientation is given along the curve so that we may speak of the "left" and "right" states at a point, the "next" and "previous" bonds on a curve and the "start" and "end" points of a curve or a bond.

The points where curves intersect (or self-intersect) are called *nodes*. Since the boundaries of the domain are represented by curves as well, all curves begin and end at nodes. States are assigned to the node along each incoming curve to represent the limiting values as the node is approached along each side of the curve.

Nodes correspond to wave interactions and can be identified by the number and type of waves meeting there. For example, during the initial refraction of the shock in the Richtmyer-Meshkov calculations the incident shock, incident

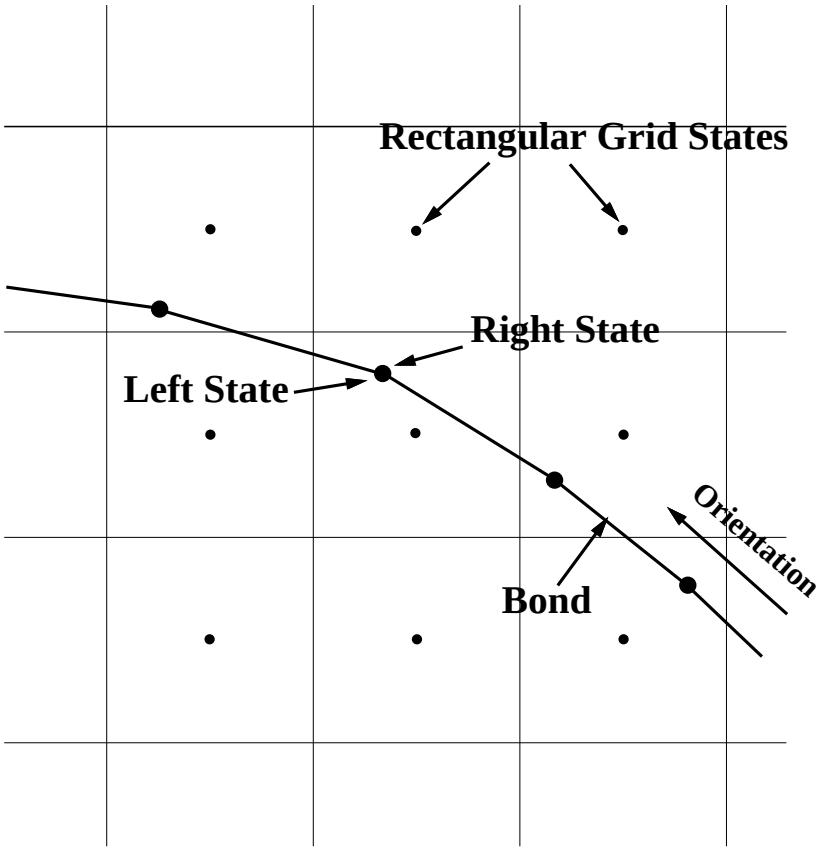

Figure 3.2: Schematic representation of the grids used in front tracking. A one dimensional curve is embedded in a two-dimensional rectangular finite difference grid. The curve is piece-wise linear with state data on each side of the points. An orientation is assigned which defines right- and left-hand states.

contact, transmitted shock, deflected contact and reflected waves all meet at a single point where the incident shock is refracted by the material interface. This is known as a *refraction node*. Similarly, where a tracked wave meets the boundary a *boundary node* is created. Other node types in gas dynamics include *Mach nodes* for Mach triple points and *cross nodes* at shock-shock interactions. Each node type uses a different algorithm for updating its position and states for each time step.

In addition to the states along curves we have cell-centered state values on the underlying rectangular grid. To facilitate the calculation of states at arbitrary points in the domain we perform a front-limited triangulation of the dual computational grid (formed by the cell centers) and tracked fronts (see Figure 3.3). The triangulation is constrained so that no triangle crosses a tracked front. A corner of an individual triangle is either a dual-grid corner, a point on a tracked front or an intersection between a tracked front and a lattice cell boundary. The states at these positions serve as data for a linear interpolation of the solution into the interior of the triangle. The triangulation in the front tracking code differs from other triangular representations of a flow in that the tracked waves are dynamic and the the triangulation must be regenerated at each time step.

It is not necessary to track all the waves in a given computation. In some of the simulations presented here only the contact discontinuity was tracked– the incident, transmitted and reflected waves being captured by the interior (Godunov-type) scheme.

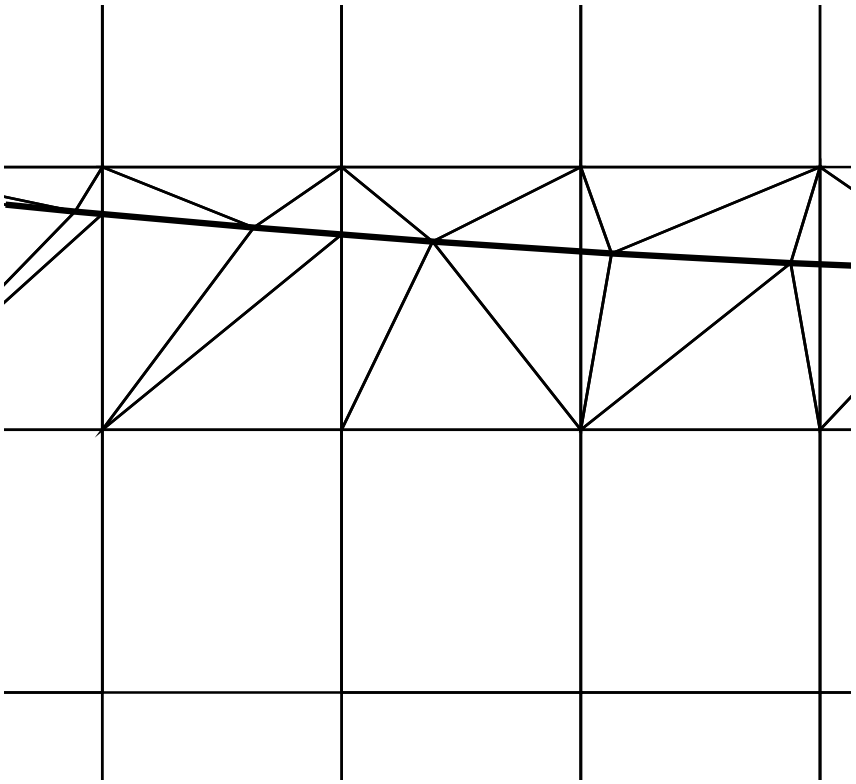

Figure 3.3: An example of the triangulation of the computational domain in the region of a tracked wave. The thick line is the tracked front. The vertices of the triangles are points on the tracked front, corners of the computational dual grid and intersections of the front with the grid. Since states are available at all vertices of a triangle the state at an arbitrary point interior to a triangle can be computed by interpolation.

3.2 A Front Tracking Time Step

A time step is done in two parts in front tracking. The first part is the propagation of the tracked fronts using front positions and states and interior states at time t to find new front positions and states on the fronts at time $t + \Delta t$. The second part of the time step is the updating of the interior (non-front) states using the new front information as boundary data. The interior states are updated using a version of Colella's Eulerian MUSCL, a second-order Godunov-type method [3, 30, 69]. Care is taken at interior states affected by the tracked waves during the time step to avoid differencing across a discontinuity.

3.2.1 Front Propagation

The front propagation is further divided into two steps: curve propagation and node propagation. Some of the following can be found in [28].

Curve Propagation

Curves are propagated by updating all non-nodal points of each curve. Normal and tangential directions to the curve are found at each point to be propagated (Figure 3.4). These directions are used to split the propagation into a normal update and a tangential update by operator splitting of the Euler equations in the form

$$u_t + \vec{n} \cdot [(\vec{n} \cdot \nabla) f(u)] + \vec{t} \cdot [(\vec{t} \cdot \nabla) f(u)] = h(u) \tag{3.1}$$

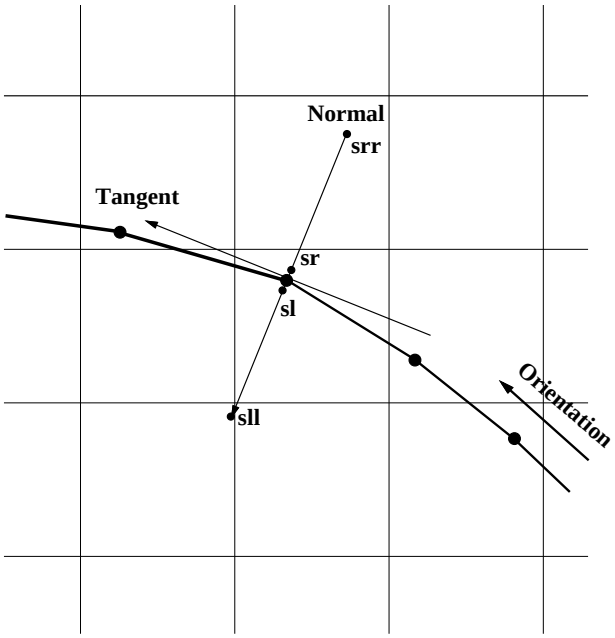

Figure 3.4: The normal and tangential vectors at a point to be propagated. The states used in the normal update computation are labeled as srr, sr, sl and sll.

where $u(\vec{x}, t)$ is the state vector, $\vec{n}$ and $\vec{t}$ are unit normal and tangential vectors along the curve, $f(u)$ is the flux and $h(u)$ is the vector of source terms, if any. It is during the normal step that the point is moved to its new location. In practice all of the normal propagations are completed before the tangential propagations.

The initial steps of a normal propagation are the same for all wave types. Right and left states, S_r and S_l, are taken at the point to be propagated, as well as two more states, S_{rr} and S_{ll}, a distance Δx in a normal direction on

the right and left sides of the curve (see Figure 3.4). Using these states a non-local Riemann problem is solved as follows. Between S_r and S_l we solve a Riemann problem and follow the wave of the proper family (contact, forward or backward shock, rarefaction leading edge or rarefaction trailing edge) to obtain an estimate of the new point position at time $t + \Delta t$. From this new position we trace back characteristics on each side of the wave to the initial data to find states there. From here we use the characteristic equations and the Rankine-Hugoniot conditions to find time-updated states at $t + \Delta t$. The particular characteristic method used depends on the wave being tracked, i.e. shock wave, contact or rarefaction edge, since each type of wave has different types of characteristic information coming into it and different jump conditions. We give here the details on the forward shock wave calculation. Other waves are propagated in a similar manner. For convenience the discussion will be limited to the case of polytropic gases.

The update of the ahead state uses the information coming in from the three ahead characteristics. Along these characteristics $\lambda_\pm : \frac{dx}{dt} = u \pm c$ and $\lambda_0 : \frac{dx}{dt} = u$ we have the following equations:

$$dw_+ = \frac{c\,dS}{\gamma R} \tag{3.2}$$

$$dw_- = \frac{c\,dS}{\gamma R} \tag{3.3}$$

$$dS = 0 \tag{3.4}$$

where the $w_\pm = \frac{2c}{\gamma - 1} \pm u$ are the Riemann invariants, S is the specific entropy, γ is the polytropic exponent and R is the universal gas constant R_0 divided by the molecular weight of the gas.

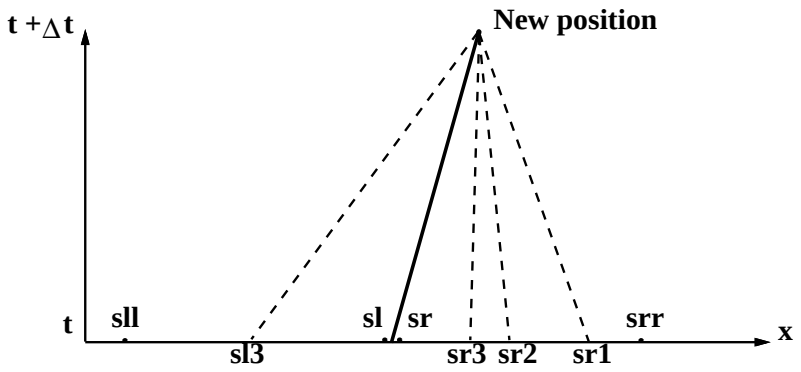

Figure 3.5: Diagram showing estimate of new wave position at time $t + \Delta t$ and traceback of characteristics to initial line.

The equations (3.2–3.4) are discretized as

$$\Delta w_{\pm} = \frac{\bar{c}\Delta S}{\gamma R} \tag{3.5}$$

$$\Delta S = 0 \tag{3.6}$$

using the states S_{r1}, S_{r2} and S_{r3} from the characteristic traceback step as initial data (see Figure 3.5). This results in nonlinear algebraic equations which can be solved for the state ahead of the shock. For the state behind the shock we use the discretized equation for the Riemann invariant w_+ along the characteristic λ_+ emanating from state S_{l3} along with the Rankine-Hugoniot conditions in the form

$$\frac{[P]}{[u]} = -m \tag{3.7}$$

$$\frac{[P]}{[V]} = -m^2 \tag{3.8}$$

$$\frac{\rho_1}{\rho_0} = \frac{\mu^2 + P_1/P_0}{1 + \mu^2 P_1/P_0} \tag{3.9}$$

where $[\cdot]$ denotes the jump in a quantity across the shock, m is the mass flux, $\rho = \frac{1}{V}$ is the density, $\mu^2 = \frac{\gamma-1}{\gamma+1}$ and the subscripts 0 and 1 denote states ahead and behind the shock, respectively. The combination of the jump conditions with a discretization of the equation along the characteristic results in four simultaneous equations which can be solved for the four state variables P_1, ρ_1, u_1 and m. These variables completely specify the behind state.

It is clear that if the discretization error of the characteristic equations (3.5) and (3.6) is $O((\Delta t)^2)$ this procedure will result in computed states with second order errors as well as long as the initial characteristic data given by S_{r1}, S_{r2}, S_{r3} and S_{l3} have errors of at most second order. To see that these states do indeed have $O((\Delta t)^2)$ errors we must show, assuming smooth flow away from the shock, that the characteristic tracebacks find initial positions correct through order Δt. These tracebacks are found by taking characteristics from the estimated shock position and the position and states at the estimated shock position are correct through first order. This means, then, that the traceback position is also correct through first order. Thus the states at the base of the approximate characteristics there have errors of second order.

Given that the number of time steps in a solution of a hyperbolic system is $O(\frac{1}{\Delta t})$ we can hope for convergence in an appropriate norm at a rate $O(\Delta t)$. This assumes that the front propagation is properly coupled to sufficiently accurate tangential and interior solvers.

An alternative scheme may also be used to propagate the shock. In this scheme the ahead state S_0 is calculated using first order discretizations of the

characteristic equations, but using them in the form

$$dP \pm \frac{du}{\rho c} = 0 \tag{3.10}$$

$$dS = 0 \tag{3.11}$$

Referring to Figure 3.6, to find the state behind the shock we first solve a Riemann problem between the states S_{l3} and S_l and let the state S_l' be the state behind the forward moving wave. This has the effect of filtering out backward moving waves. We then solve a Riemann problem between S_l' and the computed ahead state S_0, letting S_1 be the state behind the resulting forward shock wave in the Riemann solution. This new state S_1 is the updated state behind the shock.

To see that this method is consistent with the equations of motion first note that if we find the behind state by considering the discretization of the characteristic equation for the state S_{l3}

$$(P_1 - P_{l3}) + \frac{1}{\rho_{l3} c_{l3}}(u_1 - u_{l3}) = 0 \tag{3.12}$$

and combine this with the state ahead of the shock (S_0) and the shock jump conditions we will have the behind state correct through first order. To show that the Riemann solution method is consistent through first order we must show that the Riemann solutions also satisfy the jump conditions and the discretized characteristic equation (3.12), at least through first order. That the Riemann solutions satisfy the jump conditions is clear. We are left, then, with showing that they satisfy (3.12).

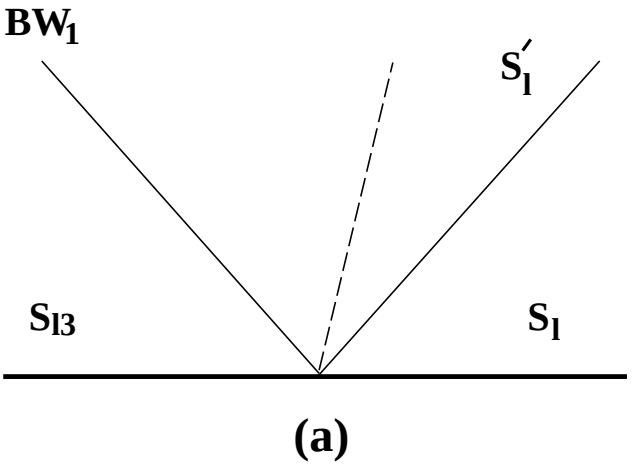

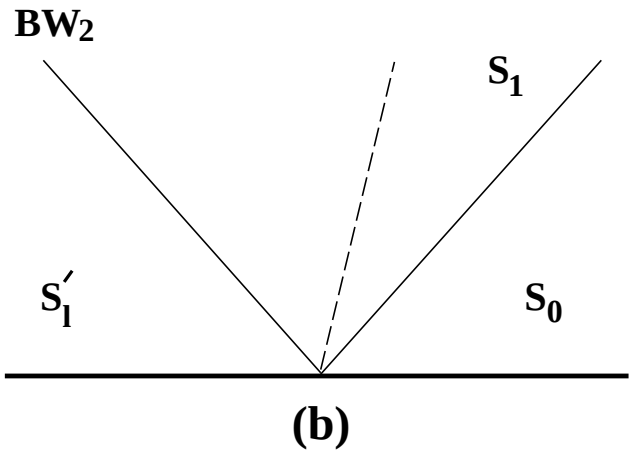

Figure 3.6: A representation of the Riemann problems solved for the alternate point propagation routine.

The backward wave from the first Riemann problem (labeled BW_1 in Figure 3.6a) will be weak for sufficiently small Δt and the transition across BW_1 can be described by the forward characteristic equation through second order whether this wave is a shock or a rarefaction. We have, then,

$$(P_l^{'} - P_{l3}) + \frac{1}{\rho_{l3} c_{l3}}(u_l^{'} - u_{l3}) = O((\Delta u)^3) \tag{3.13}$$

$$= O((\Delta t)^3) \tag{3.14}$$

Similarly, across the wave BW_2 we have the following relationship between the states $S_l^{'}$ and S_1:

$$(P_1 - P_l^{'}) + \frac{1}{\rho_l^{'} c_l^{'}}(u_1 - u_l^{'}) = O((\Delta t)^3) \tag{3.15}$$

$$= (P_1 - P_l^{'}) + \frac{1}{\rho_{l3} c_{l3}}(u_1 - u_l^{'}) \tag{3.16}$$

where the last equality follows from the fact that the state $S_l^{'}$ differs from S_{l3} by terms of third order in Δt. Adding (3.14) and (3.16) gives

$$(P_1 - P_{l3}) + \frac{1}{\rho_{l3} c_{l3}}(u_1 - u_{l3}) = O((\Delta t)^3) \tag{3.17}$$

which shows that the Riemann solution method is indeed consistent with the equations of motion, at least through first order. The method is not consistent past first order since the ahead state and the characteristic data are limited to first order.

For the tangential update at a point we do each side of the point separately. Since the finite difference scheme, MUSCL, uses a five point stencil we take two states a distance Δx and $2\Delta x$ along each side of the point on the normally propagated curve. These states are then projected onto the tangent to the

curve at that point and the finite difference scheme is used to calculate new states at that point. The point is not moved to a new position in the tangential step as it is during the normal step–only the states are updated.

Untangling the Fronts

After the normal propagation step we must check to see if there are any new intersections of tracked waves. If so the intersections must be resolved. This generally involves replacing the intersection point by a node and computing wave interactions at the new node. As an example, early in a Richtmyer Meshkov instability simulation the shock wave strikes the contact and produces a pair of shock refraction points. Nodes are created at these points and transmitted and reflected waves are created as appropriate.

Node Propagation

Each type of node has a different propagation algorithm. We will discuss the propagation of refraction nodes as these are the primary nodes of interest in the present computations.

A diagram of a refraction node is given in Figure 3.7a. In our implementation the node propagation is done between the normal and tangential curve propagation steps, so at the beginning of the node propagation all points on the relevant curves have been normally propagated except for the points at the node itself. The first step is to propagate the nodal points of the curves. This will result in a configuration similar to Figure 3.7b. Notice that the incident

shock and contact have a new intersection point. We take this intersection to be the node position at the new time and remove the parts of the curves past the intersection (frame (c)). We know the state behind the shock wave and on both sides of the contact, as well as the angle between the shock and the contact. If we move to a frame in which the node is stationary we can use shock polar analysis [32, 44] to find the angles at which the reflected and transmitted waves emanate from the node. To complete the propagation we take rays from the node at the computed angles and intersect them with the propagated curves, extending the curves slightly if necessary (Figure 3.7d).

We should note here that the CFL stability condition applies to curve and node propagations as well as to interior state calculations. We take care to ensure that Δt is small enough that the node position will not change by more than some fraction of Δx during the time step. This has important consequences when calculating refraction nodes as the node velocity can be quite large when the incident shock and contact intersect at a small angle. We have found that our front tracking calculations can take up to 10 times as many time steps during the critical refraction period as a standard shock-capturing scheme, providing enhanced stability as well as increased temporal resolution.

3.2.2 Interior States

The interior states, i.e. the states not on a tracked wave, are propagated using the above mentioned operator-split MUSCL scheme. In each direction we perform two passes.

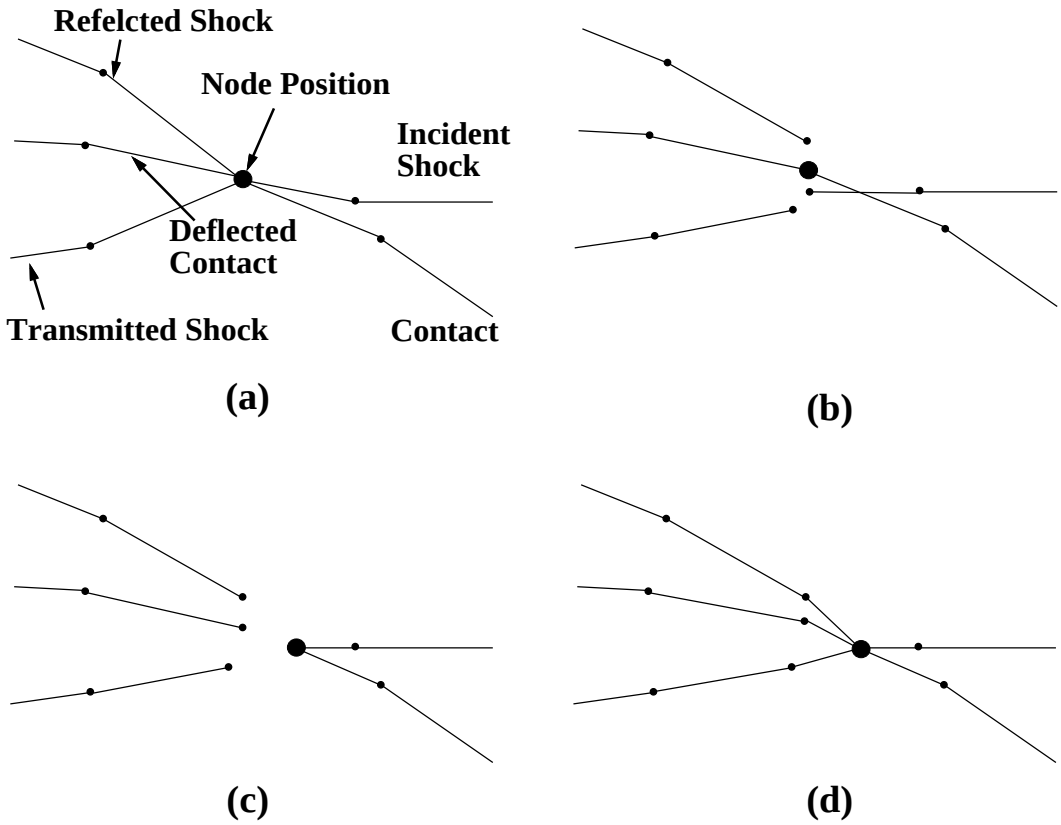

Figure 3.7: A refraction node propagation. (a) Initial configuration. (b) The points at the node are propagated in the normal direction. (c) The intersecting shock wave and contact are clipped at the new intersection point and define a new node position. (d) The reflected and transmitted waves are connected with the node at the angles determined by shock polar analysis.

In the first pass we update each interior state using only the rectangular grid, ignoring for the moment the presence of any tracked waves. For points too close to a tracked wave at either the beginning or the end of the timestep for us to get a full stencil we must make a second pass in order to avoid differencing across waves and introducing numerical diffusion. The states computed during the first pass are discarded. We then modify the stencil by taking only states which are on the same side of the tracked wave as the stencil center. We replace those stencil states that would normally come from across a tracked wave by states from the correct side of the tracked wave at the stencil/wave intersection.

By organizing the interior solver into two passes we are able to vectorize a large part of the computation. We believe that even on non-vector machines this is more efficient.

3.3 Achieving 2nd Order Accuracy

As discussed in Section 3.2.1, the normal propagation is formally first accurate. This limits the global solution to first order in the sense that if $u(x,y,t)$ is the exact solution and $\tilde{u}(x,y,t)$ is the numerical solution then $\|u(x,y,T) - \tilde{u}(x,y,T)\|_{L^2} = O(\Delta t)$ for fixed times T. Since the interior and tangential solvers are second order it would be interesting to consider the changes necessary to achieve second order accuracy.

Assuming that a second order normal propagation operator has been devised, we consider operator splitting in the context of a second order accurate

curve propagation routine. Referring to equation (3.1), we denote the second order single time step normal and tangential propagation operators by $H^k_{\vec{n}}$ and $H^k_{\vec{t}}$ where $k = \Delta t$ is the time step. We can expect second order accuracy from their combination if we apply them according to $H^{k/2}_{\vec{n}} H^k_{\vec{t}} H^{k/2}_{\vec{n}}$ or $H^{k/2}_{\vec{t}} H^k_{\vec{n}} H^{k/2}_{\vec{t}}$ (see [42] or [66]). Since the current code updates the position of the tracked wave during the normal update the latter form would be easier to implement. In a typical splitting application, a number of time steps are done consecutively which allows the half-step operators at the end of a time step to be combined with the same half-step operator at the beginning of the subsequent step. Thus n time steps would be combined into the form

$$H^{nk} = H^{k/2}_{\vec{t}} (H^k_{\vec{n}} H^k_{\vec{t}})^{n-1} H^k_{\vec{n}} H^{k/2}_{\vec{t}} \tag{3.18}$$

and require only slightly more work than a simple alternation of the tangential and normal operators. Unfortunately, however, the front tracking operators cannot be combined in this way since the tangential and normal vectors and, hence, the tangential and normal operators change at each step. This precludes the combination as in (3.18) and the scheme is required to apply the three operators at each time step. This may make splitting too expensive in a second order calculation. If so, an unsplit method would need to be devised.

In addition to the second order curve propagation routines it would be necessary to implement a second order update of interior points affected by tracked waves during the time step.

These considerations imply only formal second order accuracy. Before we could be confident that we are actually achieving this accuracy on our grids we

would need to ensure some form of stability. This should not be hard, though, since the interior scheme is quite stable, especially since the discontinuities will likely be tracked. Tracked waves will also, in general, be very stable. The only difficultly would be ensuring stability in the coupling of the interior states and the states on the tracked waves.

3.4 Diagnostics

The method of front tracking has a unique ability to precisely measure positions and states along the unstable interface. This precision is especially useful when we validate our code against the linear theory (see Chapter 8).

The most important diagnostics are the perturbation amplitude and the perturbation amplitude growth rate. The amplitude is calculated as half the difference in vertical position of the point at the center of the domain and the vertical position of a point at an edge (see Figure 1.3). Finding an edge point is simply a matter of taking either the starting or ending point of the contact (we took the start). To find the center point we loop over the points on the contact until we find the one closest to the center of the domain. Since the distance between the points on a tracked wave is typically smaller than Δx the point we find in this looping procedure will be less than $\Delta x/2$ from the true center of the domain. To calculate the perturbation growth rate we take one-half of the difference in vertical velocities at these extreme points.

The precision of this procedure is both an advantage and a possible disadvantage. While the convergence of the simulations to the correct weak solution

of the differential equations is in the spaces L^1 or L^2 we are using an L^∞ measure of the growth rate. This may causes problems as we refine the mesh (see Chapter 8). It would be useful to calculate an L^1 or L^2 measure of the growth rate and see how this changes the behavior of the simulation growth rate under mesh refinement. This has not been done at present.

3.5 Full vs. Partial Tracking

It is not necessary to track every wave in a front tracking computation. There are many possible reasons for not tracking a wave. For example, one may wish to test the effects of tracking by comparing a fully tracked simulation to one with partial tracking (this is done in Chapter 5) or to reduce the computational burden of tracking a very weak wave. Also, it is possible that a particular wave interaction may result in a configuration that is not yet implemented in our code and it would then be necessary to continue without tracking some of the interacting waves.

Our conclusion for the Richtmyer-Meshkov simulations (explored in depth in Chapter 5) is that tracking the contact is critical while tracking the shock is not as important, especially at later times. Note, though, that we must track the contact waves in order to perform our diagnostics (Section 3.4) and that contacts must separate gases with different equations of state. Note, too, that untracked shock waves are much more susceptible to post-shock oscillations that can affect the growth of the perturbation, especially slow moving shock waves as found in the air-SF_6 simulations (see Section 4.1.2).

3.6 Parallelism

Many of the simulations reported here were run on Intel Paragon and Hypercube parallel processor computers. The code uses a coarse grained parallelization via domain decomposition.

Briefly, the domain is broken into rectangles, with m rectangles down and n rectangles across. Each processor is assigned responsibility for one of the rectangles so that $m \times n$ processors are needed. Communication between subdomains is simplified by the fact that we are using an explicit method. Thus for each domain we need only append three buffer zones (for a five point stencil) on the edges that meet a neighboring domain. These buffer zones are used as data for the updating of the domain states, but updating states represented by the buffer zone remain the responsibility of the neighboring domain.

At the beginning of the timestep each processor has a full copy of states and tracked waves in its domain and buffer zones. The front propagation proceeds normally except that we do not concern ourselves with propagating the boundary nodes at the edges of the buffer zones. After the front propagation there is a synchronization step during which neighboring processors pass the front information necessary to update buffer zones with respect the new front positions and states. Next, the interior states are propagated and another communication is made to update the interior states in the buffer zones.

We found excellent performance using this method of parallelization with an almost linear increase in speed as we added processors. The largest run

(an air-SF_6 simulation with a mesh of 250 zones by 1500 zones) ran for approximately 80 hours on 32 Paragon processors with 32MB of RAM each. For comparison a 62 by 384 simulation took 15 hours on a Sun SparcStation 2 for the same simulation real time.

Chapter 4

Simulation Results

In this chapter the front tracking simulations of Benjamin's 1993 air-SF_6 experiments [6] and Meshkov's air-helium experiments [54] are presented. The simulations are validated in Chapter 8 and the results are analyzed in detail in Chapters 5 and 7.

4.1 Computational Issues

There are various computational issues common to both of the experiments we simulate. These issues are discussed in the following sections.

4.1.1 Domain

Rectangular domains are used with flow-through boundaries at the top and the bottom and periodic boundaries at the sides.

While the flow-through boundaries are exact for steady flow, they are not exact for unsteady flows and signals may propagate back into the domain after the transmitted and reflected waves pass through the bottom and top

boundaries, respectively. The domain is long enough that no signals reach the contact during the period of interest. In addition, the contact is initialized at a level which maximizes the time before boundary contamination.

For the air-SF_6 simulations a domain of 3.75cm by 22.5cm is used. Since the sound speed in SF_6 is so much smaller than in air the contact is placed at a position 5.5cm above the bottom boundary to further reduce the chance of boundary signal contamination. The domain length and contact position are determined from an analysis of the 1D unperturbed problem and are sufficient to guarantee that boundary signals would not affect the computation until at least 900μs, which is later than the simulation stopping time of 850μs. Indeed, there is no evidence of boundary signals in the growth rate. The domain length chosen appears to be optimal since if the domain length is reduced there are changes in the growth rate curve as a result of boundary signals while there is no change if the domain is lengthened.

The air-SF_6 simulations used various mesh sizes from 62 zones per wavelength to 250 zones and the simulations appear to converge at the level of 125 zones per wavelength. This is approximately the same resolution used in the simulations of the same experiment as given in [6].

The 125 and 250 zone/wavelength air-SF_6 simulations were run on an Intel Paragon. The computational time was approximately 16 hours using 16 processors for 125 zones.

The air-helium simulations used a domain of 4cm by 30cm. Since the sound speed in helium is much larger than in air the contact was placed with

its midline at an optimal position 19.9cm above the bottom boundary. The domain length and contact position were sufficient to guarantee that boundary signals had not affect the computation until at least the simulation completion time of 300μs. There is no evidence of boundary signals in the growth rate.

Various mesh sizes were used for the air-helium simulations, from 50 zones per wavelength to 200 zones, and the the growth rates have converged at the level of 100 zones per wavelength. The 100 and 200 zone/wavelength simulations were run on an Intel Paragon with a computational time of approximately 12 hours using 16 processors for 100 zones.

4.1.2 Moving vs. Lab Frame

It is most convenient to use a frame of reference which moves with the average contact position. This not only makes it easier to follow perturbation growth with time, but it allows a somewhat smaller domain without increasing the possibility of boundary signals. The frame velocity is calculated by solving the 1D (unperturbed) shock-contact interaction, i.e. a Riemann problem, and finding the velocity of the contact. This is found to be an excellent estimate of the net perturbed contact velocity.

Moving with the contact is problematic when using untracked shock waves in the air-SF_6 simulations. The low wave speed with respect to the grid of the transmitted SF_6 shock is reduced even further by the change of reference frame. This results in post-shock oscillations that affected perturbation growth by creating secondary instabilities along the contact. The problem disappears when some of the vertical velocity subtracted from the states is added

back. This nonlinear instability at slow moving waves is well-known; see, for instance, [31]. Because of this oscillation the lab frame is always used when working with untracked shocks. Note that there is no problem with tracked shocks–there is no change in the results whether the lab frame or a moving frame is used.

4.1.3 Artificial Viscosity

The front tracking code has the option to use upwind and slope-limiting artificial viscosities [30, 31] in the MUSCL solver. This is in addition to the slope limiter built into the solver [30, 69]. Since the most unstable parts of the simulation are tracked (shock waves and contacts) it is not necessary to add secondary artificial viscosities for the fully tracked runs. It is necessary, though, to use small amounts when working with untracked shock waves. However, when similar amounts of viscosity are added to the fully tracked versions no difference in calculated perturbation growth rates is found, so we are confident that the viscosities do not adversely affect the partially tracked simulations.

4.1.4 Full vs. Half-Wavelength

All of the simulations are performed using a full perturbation wavelength as depicted in Figure 1.3. We would prefer to take advantage of the natural symmetry in the problem and work with only a half-wavelength. However, this requires replacing the periodic boundaries with reflecting boundaries which causes small changes in the perturbation growth at the boundaries. Since it is at exactly these place that the amplitude is measured this causes unacceptable

changes in growth rates. This is partially due to the ill-posedness of our growth rate measure (see Section 3.4). Thus the simulations used a full wavelength.

4.1.5 Artificial Surface Tension

The interface between the fluids of interest is susceptible to secondary Kelvin-Helmholz instabilities arising from the velocity shear across the interface, especially with the sharp interfaces in a front tracking computation. Small irregularities on the interface grow exponentially and in some cases, depending on the gases and incident shock strength, are so obvious visually that there is concern that they may be affecting the large scale dynamics of interest. This is especially important as the mesh is refined since the growth rate exponents are inversely proportional to the wavelength of the perturbations which are on the order of the grid size. In order to reduce these instabilities a small amount of artificial surface tension can be introduced to the interface.

To determine the proper amount of surface tension we appeal to the incompressible small amplitude theory (see [26], sec. 101). This theory predicts that given a surface tension T a mode with wavenumber k will be stable against shear instabilities if

$$\alpha_1 \alpha_2 U^2 \leq \frac{kT}{\rho_1 + \rho_2} \tag{4.1}$$

where the ρ_i's are the densities on each side of the interface, $\alpha_i = \frac{\rho_i}{\rho_1 + \rho_2}$, and U is the velocity shear on the interface. Since we are primarily interested in instabilities with wavelengths that are a small multiple of the mesh spacing it is convenient to transform inequality (4.1) to

$$T \geq \frac{\rho_1 \rho_2 U^2 \beta \Delta x}{2\pi(\rho_1 + \rho_2)} \tag{4.2}$$

where β is the wavelength of the instabilities we wish to suppress in units of Δx, typically 2-3. Notice that all modes with smaller wavelengths will also be suppressed. Note also that the right hand side of (4.2) $\rightarrow 0$ as $\Delta x \rightarrow 0$.

Setting the T according to (4.2) does a good job of suppressing small scale instabilities. However, even when the appearance of the interfaces smooths considerably the growth rates do not change so we choose not to use any surface tension.

4.2 Air-SF_6 Experimental Parameters

Benjamin's shock-tube experiments consisted of a shock in air incident on an interface with SF_6. As mentioned in Chapter 2, a thin, perturbed membrane separates the air and SF_6 section of the tube. Amplitude data is taken by shadowgraph equipment.

The important experimental parameters are given in Table 4.1. As the experiments were conducted at Los Alamos, pressures and densities have been adjusted to compensate for the altitude. In addition to these physical parameters it is necessary to find the time period over which Benjamin took data. While he does not explicitly state the period of observation we can infer from Figure 4 in [6] that the range of times was approximately 300μs to 770μs.

Figure 4.1 shows the interface at four times during the simulation. In this figure the shock wave is moving downward from air into SF_6 and it shows

Quantity	Units	Symbol	Value
Perturbation wavelength	cm	λ	3.75
Perturbation amplitude	cm	$a(0-)$	0.24
Wave number	cm^{-1}	k	1.675
$ka(0-)$			0.4
Initial density	g/l	ρ_{air}	0.95
	g/l	ρ_{SF_6}	4.84
Initial pressure	bar	P	.8
Shock strength	Mach number	M	1.2
Ratio of specific heats		γ_{air}	1.4
		γ_{SF_6}	1.09

Table 4.1: Air-SF_6 Parameters

the interface at $t = -13\mu$s (where $t = 0$ corresponds to the end of the shock refraction), 132μs, 567μs and 857μs. Notice how the interface appears to be relatively sinusoidal at $t = 132\mu$s while at 567μs the heavy SF_6 spike is narrowing and the air bubbles are broadening. At $t = 857\mu$s we see the beginnings of mushroom caps formed by a rollup of the interface.

4.3 Air-SF_6 Perturbation Growth

The perturbation growth history is presented in Figures 4.2 and 4.3. These figures compares the amplitude and growth rate predictions of the front tracking simulation, experiment, impulsive model and linear theory.

To facilitate comparison with experiment a least-squares analysis of the amplitude data is performed over the experimental interval of 300μs to 770μs in order to find a single growth rate. The computed growth rate is 9.2m/s which compares quite well with the experimental growth rate of 9.18m/s. The

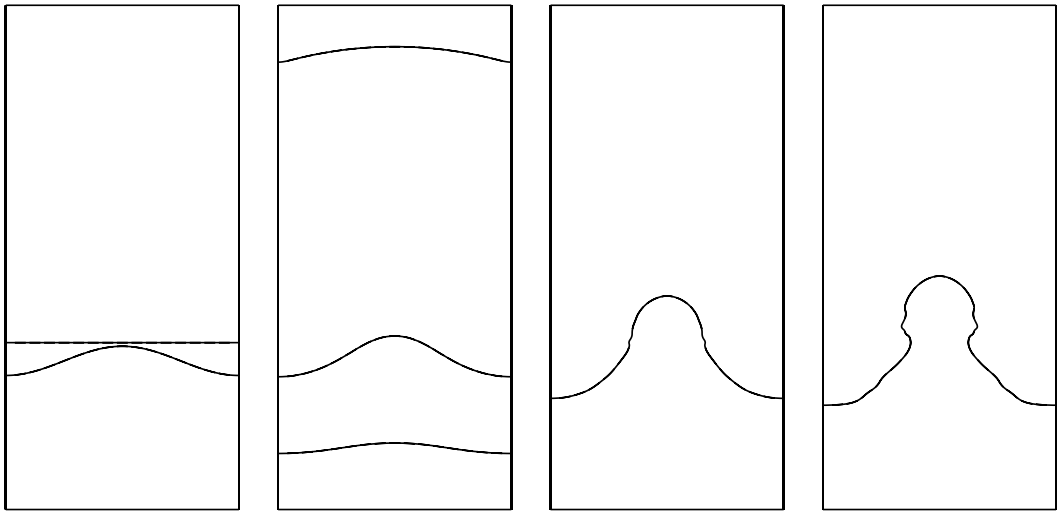

Figure 4.1: The air-SF_6 interface at different times during the simulation (a) $t = -13\mu s$ ($t = 0$ corresponds to the completion of the shock refraction) (b) $t = 132\mu s$, (c) $t = 567\mu s$. Notice that the interface is becoming non-sinusoidal as the SF_6 spike begins to narrow and the air bubble begins to broaden. (d) $t = 857\mu s$. Mushroom caps are developing due to vorticity along the interface.

linear and impulsive models agree well with each other with the linear theory predicting a growth rate of 16.5m/s and the impulsive model predicting 16.1m/s, but these growth rates are approximately twice as large as found through experiment and simulation.

The simulation amplitude is somewhat larger than found through experiment. Since the computed growth rate agrees so well at experimental time we must conclude that the difference lies in the high growth rate computed at early time. Chapter 5 discusses the agreement between experiment and simulation.

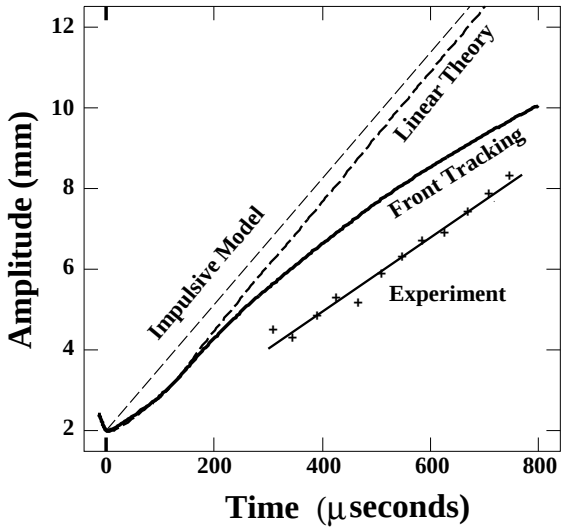

Figure 4.2: Perturbation amplitude, $a(t)$, of the shocked air-SF_6 interface. This graph compares the results of experiment, front tracking simulation, linear theory and Richtmyer's impulsive model. The plus marks (+) show the results of one particular experiment

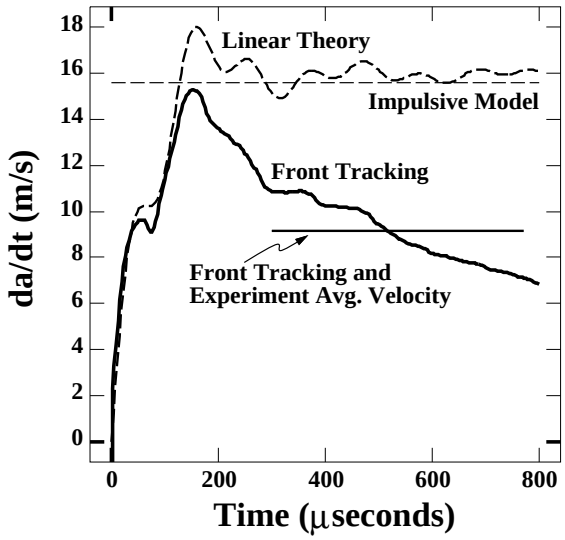

Figure 4.3: Perturbation growth rate, $\dot{a}(t)$, of air-SF_6 interface. In addition to the front tracking, linear theory and impulsive model results this figure shows the results of a least squares fit to the front tracking amplitude data over the period of experimental observation.

Quantity	Units	Symbol	Value
Perturbation wavelength	cm	λ	4.0
Perturbation amplitude	cm	$a(0-)$	0.2
Wave number	cm^{-1}	k	1.57
$ka(0-)$			.314
Initial density	kg/m^3	ρ_{air}	1.2
	kg/m^3	ρ_{helium}	0.167
Initial pressure	bar	P	1.013
Shock strength	Mach number	M	1.52
Ratio of specific heats		γ_{air}	1.4
		γ_{helium}	1.63

Table 4.2: Air-Helium Parameters

4.4 Air-Helium Experimental Parameters

Meshkov's experiments consisted of a shock in air incident on an interface with helium. A thin (1μm thick) nitrocellulose membrane separates the air and the helium. Schlieren photographs are taken at regular intervals to obtain a time history of the perturbation growth. Relevant experimental data are listed in Table 4.2.

The amplitude data is given in [54] as a function of the contact's translational distance down the shock tube with data given for the range of 5.2cm to 10cm. While the results here could also be stated in terms of translation distance it is easier to compare to other simulations if we state results as functions of time. Using the 1D unperturbed theory as a guide the translational velocity is found to be 351m/s. Thus the observation period is found to be 150 to 280μs after the shock has completed its refraction through the contact.

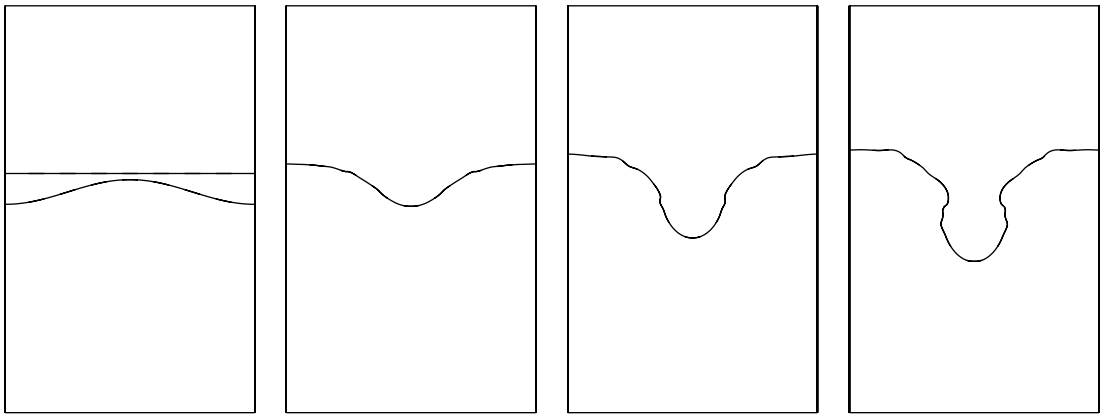

Figure 4.4: Air-helium interface: a) $t = -10$, b) $t = 90\mu s$, c) $t = 190\mu s$, and d) $t = 290\mu s$ using 100 zones/wavelength.

Figure 4.4 shows the interface at four times in the simulation. The shock wave is moving downward from air into helium. As expected there is an early interface inversion followed by perturbation growth. The air spike has narrowed considerably by 90μs and this narrowing continues in the later frames.

4.5 Air-Helium Perturbation Growth

Figures 4.5, 4.6 and 4.7 show the perturbation growth results. These figures compare the amplitude and growth rate predictions of the front tracking simulations, experiment, impulsive model, linear theory and simulations of Meyer and Blewett [56].

As with the air-SF_6 simulations a least-squares analysis of the amplitude data is performed over the experimental interval of $150\mu s$ to $280\mu s$ to find a single growth rate. The computed least squares growth rate is 25m/s which is approximately 55% larger than the experimental value of 16m/s. However, the value reported by Meyer and Blewett, 47m/s, is three times the experimental value. As can be seen in Figures 4.6 and 4.7, the front tracking simulations

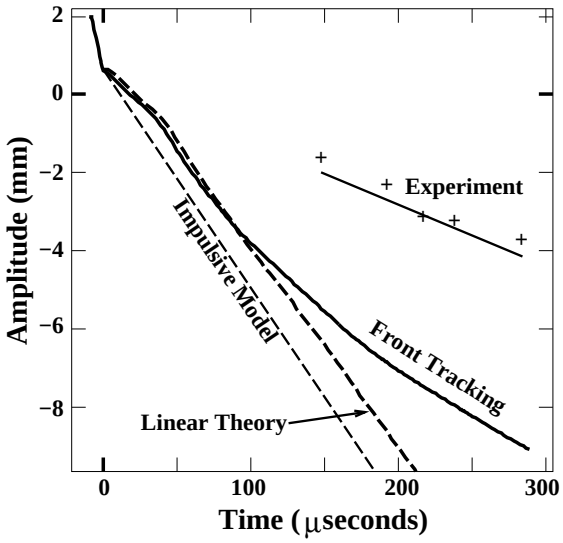

Figure 4.5: Perturbation amplitude $a(t)$ of the shocked air-helium interface. The graph shows the amplitudes from experiment (+), front tracking simulation (FT), linear theory, impulsive model.

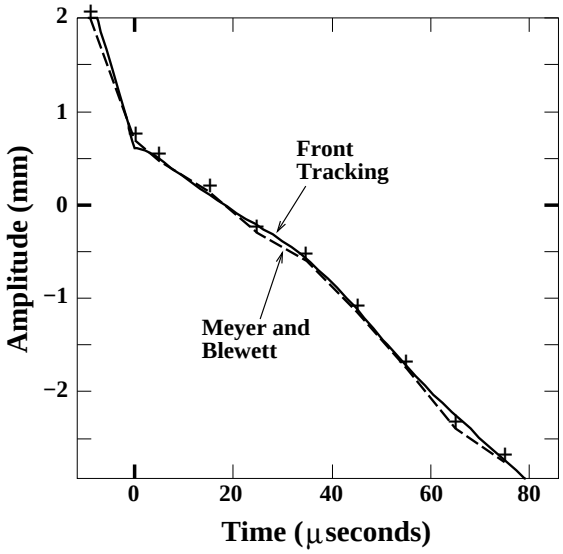

Figure 4.6: An enlargement of amplitude graph. This figure shows the early time agreement between the front tracking simulations and those of Meyer and Blewett (+).

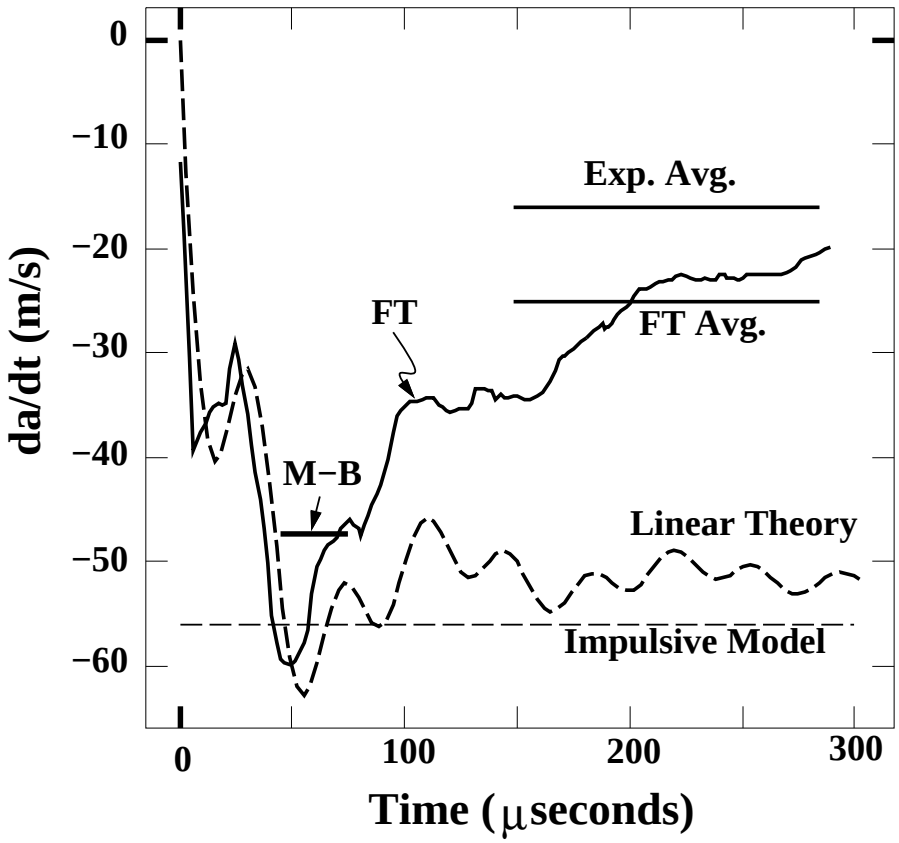

Figure 4.7: Perturbation amplitude growth rate $\dot{a}(t)$ of a shocked air-helium interface. We show the growth rates from front tracking simulations, linear theory, impulsive model and the simulations of Meyer and Blewett (marked M-B) as well as the experimental average and the best-fit estimate from the front tracking amplitudes.

agree well over the early-time interval for which Meyer and Blewett have simulation data. The difference in reported growth rates is due to the fact that they measure the growth rate much earlier than the experimental time and catch the early time peak in growth rate. Much more is said on the subject in Chapter 5.

The linear and impulsive models agree well with each other, but the growth rates are much larger than those found through experiment and simulation. The impulsive model predicts a growth rate of 56m/s while the linear theory asymptotic growth rate is 51m/s.

The computed amplitude is larger than found through experiment. Again, as with the air-SF_6 simulations, since the computed growth rate agrees well at experimental time we must conclude that the difference lies in the high growth rate computed at early times $t < 100\mu$s. We have more to say on the agreement between experiment and simulation in the next chapter.

Chapter 5

Agreement with Experiment

As mentioned in Chapter 1 previous simulations of the Richtmyer-Meshkov instability have predicted growth rates up to 200% too large when compared with experimental results. In Chapter 4 the growth rate results of front tracking simulations were presented which were much closer to the experimental growth rates than the previous simulations. Indeed, the simulations of the air-SF_6 experiments of Benjamin predicted the experimental growth rates exactly while the simulations of Meshkov's air-helium experiments were only 55% larger than experiment while previous simulations of the same experiments were 200% too large. We believe there are two factors involved in this improvement. First, the increased resolution and lack of numerical diffusion with provided by front tracking are necessary to correctly model the experiments and, second, the growth rates are measured only during the period of actual experimental measurement.

The failure of theory to agree with experiment is discussed later, in Chapter 7.

5.1 Role of Front Tracking

To test the effects of tracking, the air-SF_6 simulations were run with the tracking of certain waves disabled. The untracked waves, then, were captured by the underlying finite-difference scheme. It is necessary to use a tracked contact wave to separate gases with different equations of state, so the interface is always tracked. It is possible, though, to selectively untrack the other waves in the problem to judge their effects. For this test, for example, simulations were run without the transmitted shock, the reflected shock or both. The simulation was also run with the incident shock untracked. Note that with an untracked incident shock there is no tracking of the waves scattered from the shock refraction so that only the contact wave was tracked. Even with this minimal amount of tracking there is very little difference in the computed growth rates. In Figures 5.1 and 5.2 we see a superposition of the growth rate and amplitude curves found using an untracked incident shock and the curves for the fully tracked simulations. It is clear that untracking the shock has relatively little effect on the simulations even at very early times when the transition width of the shock wave is expected to have its greatest effect. In fact, the two growth curves are almost identical and the slight difference in growth rates has little effect on the amplitude.

We conclude from the agreement between the fully tracked and the partially tracked simulations that the important element in correctly computing the growth rates is the tracking of the interface itself. There are several possible reasons for this. First, there is no numerically generated mass diffusion

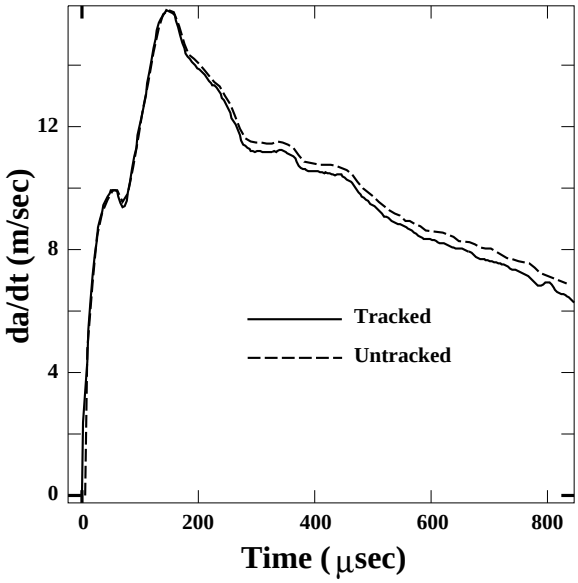

Figure 5.1: Growth rate graph for air-SF_6 simulations with untracked incident shock superimposed on graph for fully tracked simulation. There is little difference between the simulations.

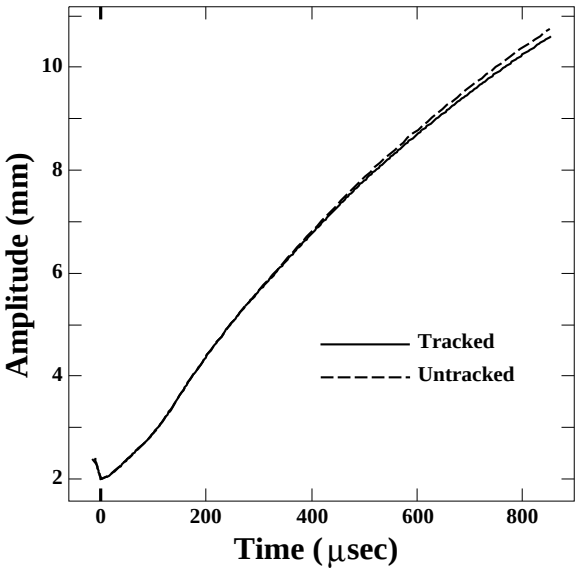

Figure 5.2: Amplitudes for air-SF_6 simulations with tracked and untracked incident shock waves. The small differences in growth rate accumulate, but the amplitudes are quite close.

or smearing of the interface. We believe this to be particularly important. Second, the vorticity along the interface which drives the instability is sharply captured by the front tracking method. Finally, front tracking has an unsurpassed ability to measure interface positions and velocities. We believe that a combination of these factors lead to the improved agreement with experiment.

Menikoff [53] has suggested that a shock refraction can lead to entropy errors at the contact due to the artificially larger shock width. In the front tracking simulations with an untracked incident shock wave there were no detectable entropy errors. Either this simulation is not susceptible to such errors or the method used to track the contact eliminates them.

5.2 Role of Timing

In Chapter 4 the front tracking results for Meshkov's air-helium experiments are compared to those of Meyer and Blewett [56]. As can be clearly seen in Figure 4.6 the front tracking results agree quite well with theirs, yet they quote a growth rate of 47m/s which is 200% larger than the experimental value of 16m/s experiment while the front tracking simulations predict a growth rate only 55% larger, 25m/s. This difference is due mainly to the difference in periods of growth rate measurement. The front tracking growth rate measurements are made during the experimental time period after there has been a significant decay in growth rates from an early time peak. By only simulating the first 80μs of the experiment (and, hence, stopping before any experimental data is taken), Meyer and Blewett made their measurements squarely in

the middle of the high growth period. This is clear from Figure 4.7. The front tracking least squares estimate of the velocity during this time period is 53.5m/s.

It should be noted that the amplitude vs. time data given by Meyer and Blewett is inconsistent with their quoted growth rate. A least squares growth rate estimate taken from their amplitude data gives a growth rate of 55m/s, as does a direct measurement of the slope of their best-fit line. The reason for this inconsistency is unknown.

As with the air-helium simulations, in the air-SF_6 case the experimental time period, 300μs to 770μs, is used for measuring growth. A different measurement period results in a different growth rate. For example, if the measurement is made during the period between 150-620μs the growth rate increases from 9.2m/s to 11.0m/s.

It is almost universal in the literature for authors to quote a single growth rate figure for Richtmyer-Meshkov unstable interfaces without any details regarding its determination. While this is likely to be motivated by the single growth rates that have been found in experiments and predicted by the impulsive model there is no way to know how these authors have calculated their growth rates. It is possible that these authors have not measured their growth rates at the proper time and thus overstated growth rates, as was the case with Meyer and Blewett.

5.3 Amplitude Disagreement

While there is good agreement between the simulations and experiment in terms of the perturbation growth rates, there is still a discrepancy between the simulation and experimental amplitudes. Looking at Figure 4.2 we see that the front tracking amplitude curve and the experiment best-fit line are parallel, which is to be expected since the velocities agree during that time period, but the amplitude predicted by the front tracking simulation is approximately 1.5mm too large. Similarly, Figure 4.5 shows that there is an offset of approximately 3mm between the simulation amplitude and the experimental best-fit at the beginning of the observation period.

The amplitude disagreement must be due to a lower experimental growth rate during the pre-observation period since we have good agreement during the observation period. Figures 4.3 and 4.7 show an extreme peak in simulation growth rates before the observations take place and the most reasonable explanation of the discrepancy in amplitudes is that the experimental growth rates simply do not experience this peak. There are several possible reasons for this. The first possibility is that diffusion across the membrane before the shock refraction has affected the early time growth. Benjamin [6] states that there appears to be pre-shock diffusion in some of his experiments while Sturtevant also describes problems with diffusion across membranes in his experiments [67]. Another possibility is that the material strength properties of the membrane retard early time growth. It is also possible that the membrane fragments are accelerating the mixing of the gases and this post-shock diffu-

sion is affecting the growth. Unfortunately, we cannot be sure what causes the amplitude difference until we have early time experimental data. Lacking this data it would be helpful to have simulations which simulate both pre- and post-shock mass diffusion in order to assess the possible effects.

5.4 Translational Velocities

In addition to perturbation growth rates it is instructive to consider interface translational velocities, where the interface velocity is defined to be the average of the velocities at the tip of the spike and of the bubble measured in the lab frame. While Meshkov does not report translational velocities, Benjamin [6] quotes an interface translational velocity of 85m/s for his air-SF_6 simulations. The front tracking simulations predict a velocity 24% smaller, 65.1m/s during the experimental observation period (see Figure 5.3). For comparison the translational velocity of an unperturbed interface is calculated through the solution of a 1D Riemann problem and the predicted velocity is 66.8m/s, slightly larger than the front tracking prediction. The unperturbed translational velocity is expected to be larger than the perturbed velocity based on mass conservation since the SF_6 spike, being narrower than the air bubble, will move faster than the bubble. Since the spike motion is opposite the overall motion of the contact it reduces the translational velocity.

The simulations of Benjamin et al. [6] also show translational velocities slightly below the 1D prediction and they attribute it to pre-shock diffusion across the membrane. In an attempt to measure the effects of diffusion on

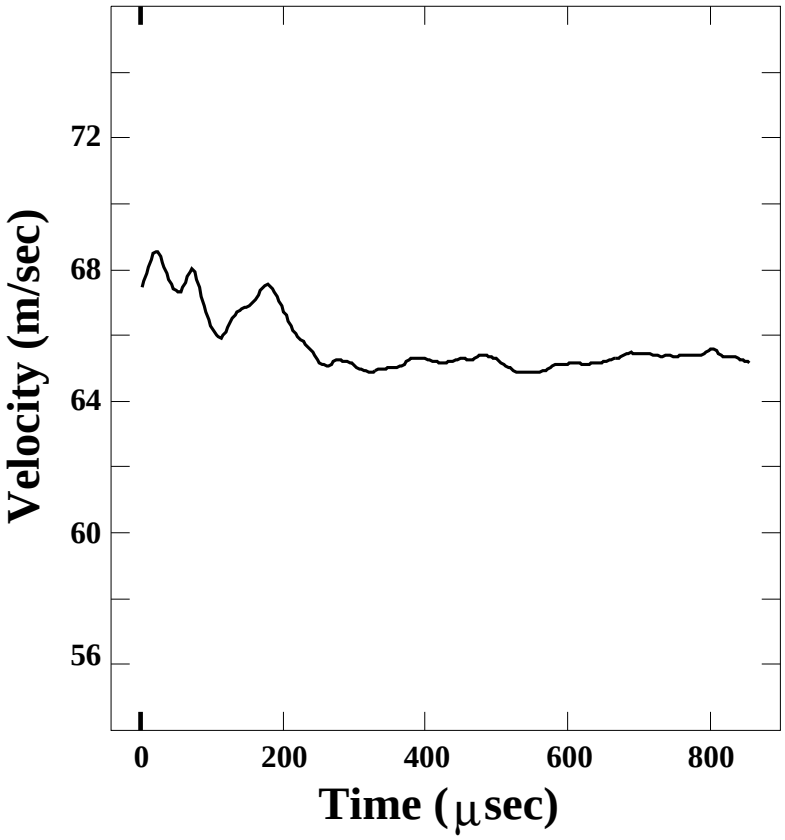

Figure 5.3: Contact translational velocity for the air-SF_6 simulation.

translational velocities a 1D simulation was run using the experimental gas and shock parameters except that the sharp interface was replaced by a transition region of linearly increasing density and constant pressure. Different transition lengths were used and the effects on the translational velocity were measured. No significant changes in velocity were found and we failed to confirm diffusion as a possible cause of the velocity difference.

It is important to understand the velocity discrepancy since it may hold clues to the unresolved difference in amplitudes.

Chapter 6

Asymptotic Behavior

6.1 Decay

A striking feature of the growth rates shown in Figures 4.3 and 4.7 is a significant decrease in the numerical growth rate from an early peak while experiment, linear theory and the impulsive model predict nearly constant rates. As can be seen in Figures 6.1 and 6.2, the decay continues to late time for the air-SF_6 case. This decay was noted by Benjamin, Besnard and Haas [6] and taken to be numerical in origin. It is our belief, though, that the decay is a real effect and is a feature of the solution of the Euler equations.

The decay in growth rates appears to be real for several reasons. First, while a decaying growth rate was not observed in the experiments we simulate other experiments, notably those of Meshkov [55], Aleshin et al. [1] and Zaytsev et al. [72], do show decaying growth rates. Decay is also seen in the simulations of Meyer and Blewett [56], Blewett [10] and Samtaney [64]. In addition, the potential flow model of Hecht et al. (section 6.2) predicts a decay in the bubble velocity for the case of a reflected shock (which is true for air-SF_6). Another

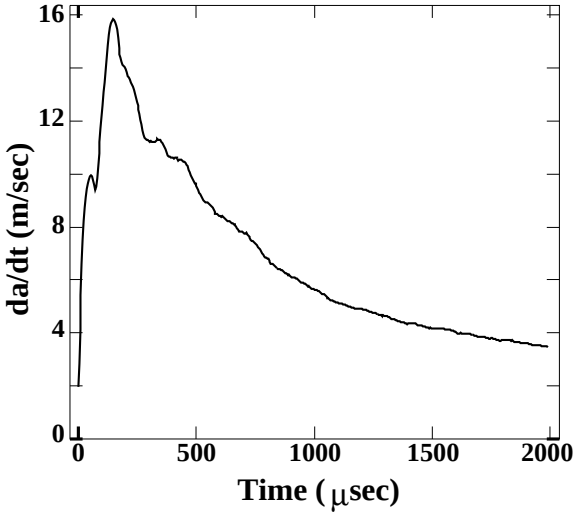

Figure 6.1: Growth rate results of long time air-SF_6 simulation. This simulation runs to a time approximately 2.5 times the end of the experiment.

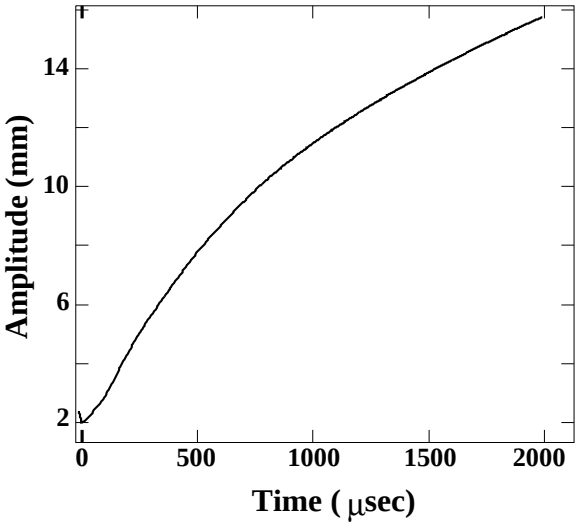

Figure 6.2: Amplitude results of long time air-SF_6 simulation.

feature of the simulations which suggest that the decay is that the decay is independent of mesh size. While the overall level of the growth rate changes with the mesh the decay rate is invariant (see Figure 8.6) when the effects of numerical diffusion should decrease with Δx. Finally, as nonlinear effects become important, especially the roll up along the sides of the interface evident in the last frame of Figure 4.1, we expect the growth rate to suffer as more energy is put into the smaller scale motion.

It is our conclusion, then, that the decay in interface growth rates is a real effect and not a numerical artifact. The decay is a very important feature of the simulations and without it there would be no agreement between the front tracking simulations and experiment. Of considerable interest, then, is the reason for the lack of decay in the experiments simulated here. While we cannot be sure, it is possible that some of the diffusion effects in the experiments that are believed to reduce the early time growth (section 5.3) affect the late time decay. New simulations and experiments are necessary to test this.

6.2 Bubble Velocity

Besides considering the full perturbation growth rate it is instructive to analyze the long time bubble and spike behaviors separately.

Hecht et al. [46] have developed a model for the motion of the bubble tip in the Rayleigh-Taylor instability and extended the analysis to include the Richtmyer-Meshkov instability. Their analysis makes four assumptions: (a) that the dynamics of the bubble are determined only by the flow in the

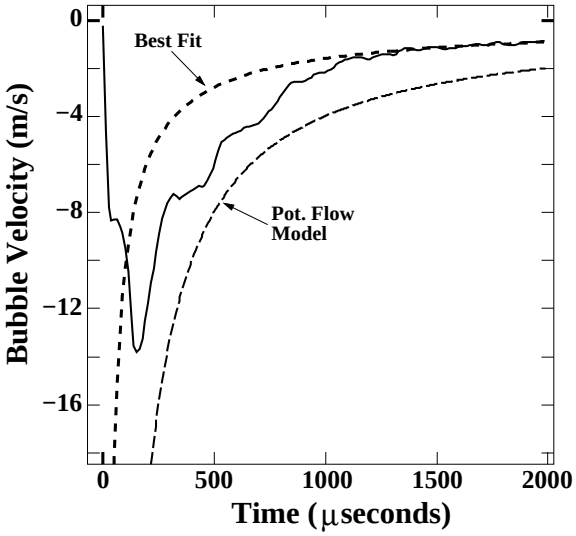

Figure 6.3: Bubble velocities for long time air-SF_6 simulation. The bubble velocity is compared against the predictions of the potential flow model.

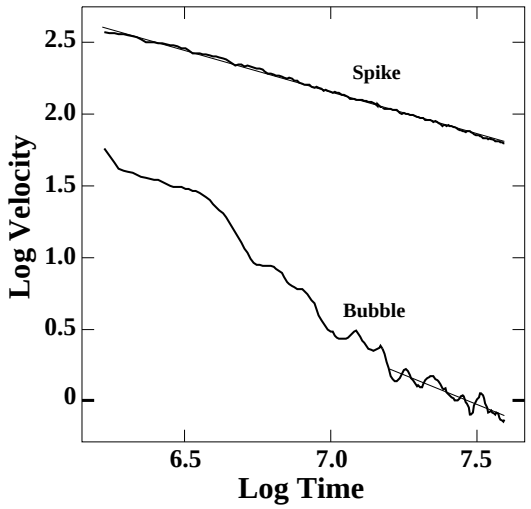

Figure 6.4: Log time vs. log velocity for bubble and spike velocities along with best fit lines.

region near the bubble tip, (b) that the flow there is irrotational, so that a velocity potential can be defined, (c) that the Atwood ratio A $\approx$ 1, and (d) that the flow is incompressible. Note that the assumption $A \approx 1$ implies a reflected shock configuration. Under these assumptions they are able to solve the potential flow equations for the bubble velocity at all times after shock refraction. While a detailed analysis of their model is beyond the scope of this work their model does lead to a simple asymptotic estimate for the bubble velocity that is easy to test. This asymptotic velocity is in the form

$$v_{bubble} = \frac{1}{3kt/2 + v_1^{-1}} \tag{6.1}$$

measured in a frame moving with the velocity of an unperturbed contact, where v_1^{-1} is an unspecified parameter with the units of velocity.

The predictions of equation (6.1) with $v_1^{-1} = 0$ are compared to the results of the long time air-SF_6 simulations in Figure 6.3. In addition, a curve fit to the data from 1350μs to the end of the simulation is superimposed. The curve is of the form $v_{bubble}(t) = ct^{-\alpha}$ where the factors $c = 437.7$ and $\alpha = 0.8135$ are determined via a linear best-fit to the log time-log velocity curve as shown in Figure 6.4. The period of the fitting is found by comparing the fits at various times and determining that they converge to the value given by beginning at 1350μs. The decay rate of the numerical simulation is of the same magnitude as that predicted from the theory, although it is slightly lower. There is an offset between the potential flow and simulation velocity curves which could be reduced by changing v_1^{-1} corresponding to a shift in time.

Note that this model applies only to bubbles and not to spikes. We empha-

size that the effects of compressibility remain important at times significantly later than the time of passage of the initial shock through the interface. Indeed, the amplitude offset is likely to be due in part to the fact that early-time compressible wave interactions discussed in Chapter 7 are not properly included in the incompressible potential flow model.

6.3 Spike Velocity

It is interesting to note that the spike velocity can also be fit by a power law. Figure 6.5 is a plot of v_{spike} and a fit of the data given by $v_{spike} = 512.9t^{-0.5836}$. As seen in Figure 6.4 the fit to the data is excellent from time $t = 500\mu$s to the end of the simulation.

The decay in bubble and spike velocities should be contrasted with the Rayleigh-Taylor instability. In the Rayleigh-Taylor case the bubble velocity approaches a constant, positive value while the spike undergoes constant acceleration [65]. This difference is surely related to the constant energy input in the Rayleigh-Taylor instability compared to the single acceleration in the Richtmyer-Meshkov instability.

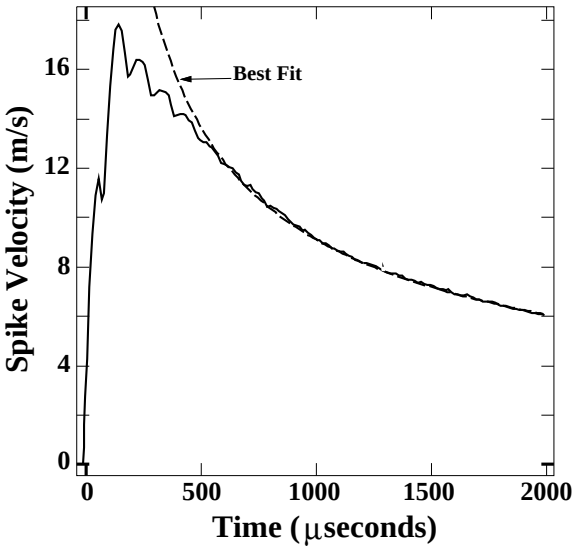

Figure 6.5: Spike velocities for long time air-SF_6 simulation.

Chapter 7

Invalidity of Theories

According to the discussion of Chapter 4, the impulsive model and linear theory seriously overstate the perturbation growth rates for both the air-SF_6 and air-helium cases. In this chapter it is shown that the simplifying assumptions made by these theories are not valid during the experimental measurement period and it is primarily for this reason that the theories disagree with experiment. Particular emphasis is placed on the assumption that the flow is linear, i.e. that it can be described by linear equations.

Similarly, it is shown that the assumption of incompressibility in the potential flow model is violated. Fraley's model is also discussed.

7.1 Simulation vs. Linear Theory

7.1.1 Air-SF_6

Referring to Figure 4.3 (reproduced here as Figure 7.1) we see that the linear theory of Richtmyer and Yang et al. agrees well with the nonlinear air-SF_6 simulations until the time that the peak velocities are reached except for a

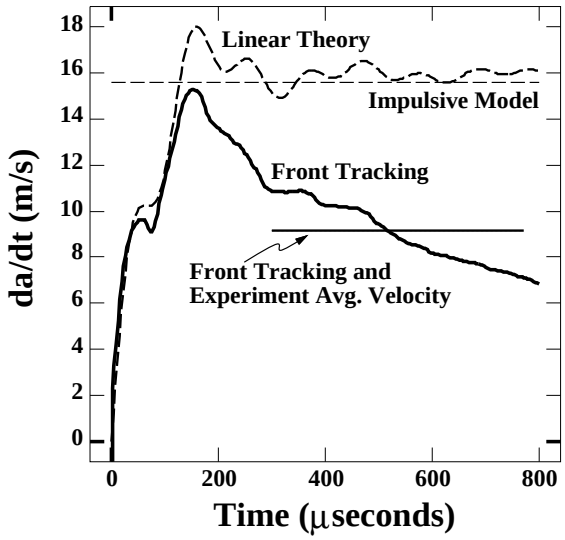

Figure 7.1: A reproduction of the air-SF_6 perturbation growth rate graph from Figure 4.3.

slight downturn in the nonlinear growth rate during the initial acceleration. Near the peak there is a quick divergence between the growth rates, with the linear theory saturating near its peak level and the simulation showing a sudden, strong downward movement. Later we see that the nonlinear simulation shows a decay in velocity while the linear theory shows no decay at all. The linear theory seriously overpredicts the growth rates at all but the earlies times because it lacks these two important aspects of the growth rate–the sudden downturns and the decay.

The sudden downturns in the front tracking simulations of the shocked interface are due to inherently nonlinear and compressible phenomena. They can be understood in terms of a series of re-accelerations of the material interface by secondary shocks whose ultimate origins are self-interactions at the reflected and transmitted wave edges. As seen in the color representations

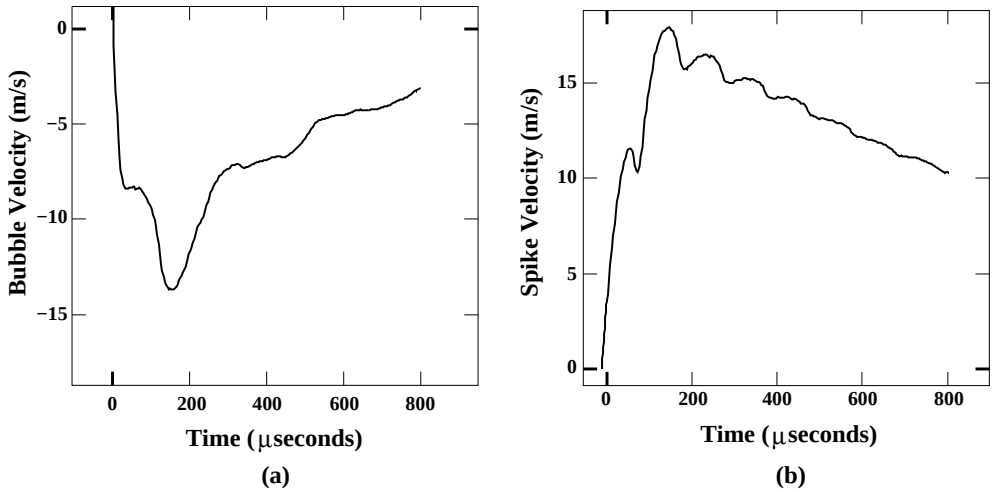

Figure 7.3: (a) Simulation air-bubble velocity (b) Simulation SF_6 spike velocity These velocities are measured in a frame moving with the interface.

of the pressure field in Figure 7.2, curvature in the reflected and transmitted waves generates additional shocks via nonlinear self-interaction. At 33μs these waves are clearly seen near the edges of the reflected shock (Figure 7.2a). As the interaction proceeds the compression fronts steepen into shocks. These shocks collide near the tip of the spike at about 68μs as seen in Figure 7.2b, producing a high pressure pulse near the interface that causes the growth rate to decline. This deceleration corresponds to the first blip in the growth rate graph Figure 7.1. At later times the waves emanating from the reflected and transmitted edges produce a series of criss-cross shock reflections. At approximately 207μs (Figure 7.2c) a strong pulse crosses the interface, leading to the severe (and permanent) deceleration of the bubble. That this decrease is due primarily to action at the bubble side of the interface is clear from a comparison of the spike and bubble velocities given in Figure 7.3. By time $t = 344\mu$s (Figure 7.2c) the strong wave action has moved away from the interface region

and the growth rate curve has smoothed considerably. Note the pair of Mach triple points at the far right of this figure.

Figure 7.4 shows pressure plots of the solution to the linearized equations and of the solution to the nonlinear Euler equations at time $t = 195\mu$s, near the time of the most severe divergence of the two solutions. We call attention to two important features of linear solutions: they do not allow the focusing of characteristics and the linearization constrains the geometry of the wave fronts to be sinusoidal. These two restrictions prevent the production of the additional shocks that are present in the nonlinear solution, i.e. there is no cascade of reflected shocks from the self-interaction of the transmitted and reflected waves. The linear solution displays a series of acoustic waves, but they do not sharpen into shocks and are thus much weaker than the corresponding waves of the nonlinear solution. Note that the strong waves in the nonlinear solution come in pairs and thus we have two pressure maxima and minima as we cross the tube in the x-direction. This is in contrast to the linear theory which in which all quantities are assumed to have sinusoidal perturbations and, hence, a single maximum and minimum value.

The analysis of secondary waves can be followed further in time to account for the plateau in $\dot{a}(t)$ during the observation period. Note that during the observational window this ringing of waves near the interface subsides. It is at this point that the hypotheses of the potential flow model begin to be satisfied, as discussed in section 7.3.

Besides the effects of the nonlinear wave interactions, the other reason for

the divergence of nonlinear theory from linear is in the overall downward trend, or decay, in the growth rate. In the nonlinear simulations the decay is seen in both the spike and the bubble velocities. (see Figure 7.3). The validity of the decay is discussed in detail in Chapter 6.

We should point out that the sharp downward movement in the nonlinear simulation at the peak growth rate is duplicated in the linear theory, although not as strongly. It appears that some of the downward motion, then, can be represented as the result of a compressible, linear wave, while the rest of the motion is due to the nonlinearity and "breaking" of the wave.

We consider the linear theory's assumption that the interface remains sinusoidal in Figure 7.5. It is clear from this figure that the interface is becoming non-sinusoidal by $t = 132\mu$s, well before the experimental observation period. The sinusoidal interface assumption also constrains the spike and bubble velocities to be the same. It can be seen in Figure 7.3 this is clearly not the case.

The behavior of the linear solution is consistent with simple order of magnitude estimates of its time of validity. We work with a dimensionless time $t_* = kc_0M_0t$, where k is the wave number of the perturbation, c_0 is the sound speed of the fluid ahead of the incident shock and M_0 is the incident shock Mach number. In terms of t_* the validity of the linear solution is

$$t_{*min} \equiv ka(0-) \ll t_* \ll 1/[ka(0-)] \equiv t_{*max}. \tag{7.1}$$

Using the experimental parameters of Table 4.1 we find that $t_{*max} \approx 2.5$ which corresponds to a time $t \approx 36\mu$s. Keep in mind that this time is by

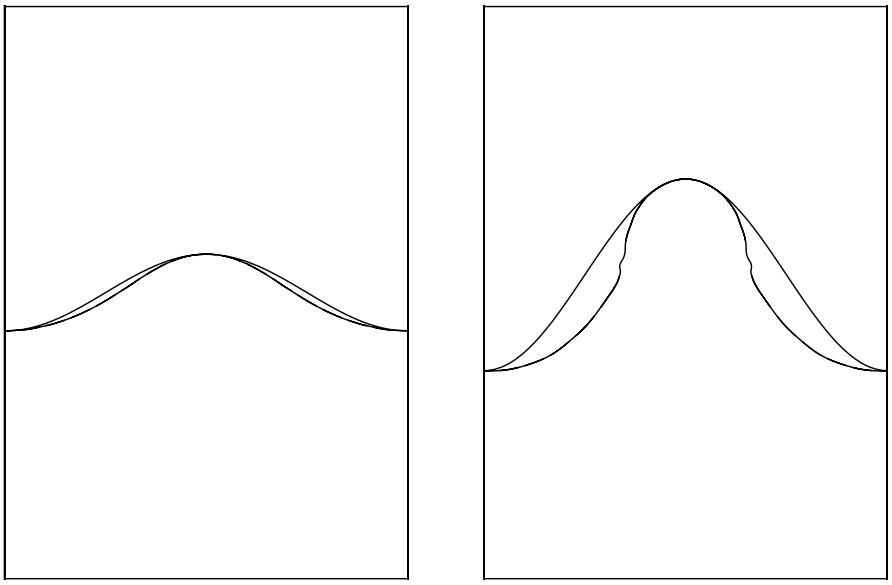

Figure 7.5: A test of the sine-shaped interface assumption of the linear theory for the air-SF_6 case. Sine waves of the same amplitude are superimposed on plots of the nonlinear interface: a) $t = 132\mu$s, b) $t = 567\mu$s.

no means rigorous. It is the result of dimensional analysis and can vary by a multiplicitive factor, but it is at least consistent with the time of validity actually observed.

The discussion regarding the comparison between the linear theory and front tracking applies to the impulsive model as well. It is interesting to note that the impulsive model and linear theory agree well in their predictions of the long time growth rate. Thus the compressibility effects included do not aid in the agreement with experiment. It is the sinusoidal interface and linearity assumptions, then, that drive the disagreement.

7.1.2 Air-Helium

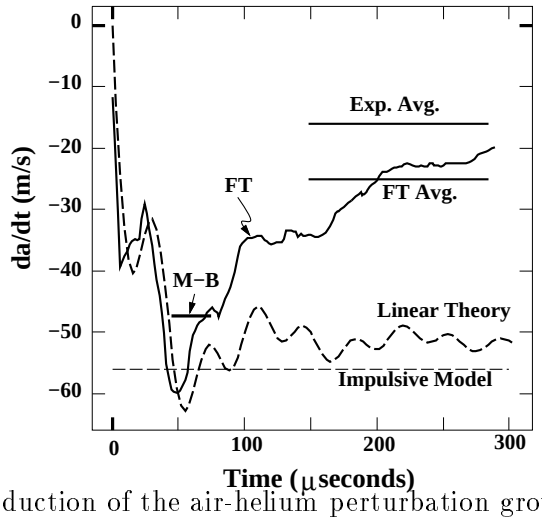

Figure 7.6: A reproduction of the air-helium perturbation growth rate graph from Figure 4.7.

As with the air-SF_6 simulations the air-helium nonlinear front tracking simulations and linear theories agree well at early times and fail to agree at later times (Figure 7.6). The disagreement again begins near the point of maximum growth rate where the nonlinear theory begins to decay while the linear theory approaches a constant value.

Figure 7.7 shows a comparison between the nonlinear and linear theories for the air-helium case. This is a plot of the pressure field at 65μs which is at the beginning of the time of rapid divergence between the growth rate predictions of nonlinear and linear theories. As with the air-SF_6 case there is a significant amount of nonlinear behavior that is not captured by the linearized theory. Specifically, the waves generated by the transmitted shock self-interaction have sharpened considerably and have probably steepened into shocks at this time. Also, there are high pressure regions forming above the bubble tips along the edges of the nonlinear simulation plot which are creating a pressure gradient

opposing the bubble motion. This gradient is not evident in the linear solution and the growth rates diverge.

We cannot validate the decay in the air-helium simulations via the potential flow model as we did in Chapter 6 since that model is valid only for the case of reflected shock. There is no reason to believe, though, that the decay mechanism for the reflected shock case will not operate in the reflected rarefaction case. This decay again results in the disagreement between the growth rate predictions of the linear and the nonlinear theories.

The early time agreement between the theories is somewhat surprising when we look at the interface profiles. In Figure 7.8 we see that during the inversion process the interface is very non-sinusoidal and remains so from that point on. The later time non-sinusoidal profiles help to explain the differences between the linear and nonlinear theories. In addition, we see in the bubble and spike velocity plots of Figures 7.9 and 7.10 that there is no symmetry in these velocities as predicted by the theory.

The inequality 7.1 suggests a validity limit on the linear equations of $t \approx 40\mu$s. This is again consistent with the observed time of agreement between the linear and nonlinear theories.

7.2 Experiment vs. Linear Theory

The nonlinear simulations and the linear theory agree at early time for both air-SF_6 and air-helium, but the linear theory seriously overstates the experimentally observed growth rate while the nonlinear simulations agree quite well

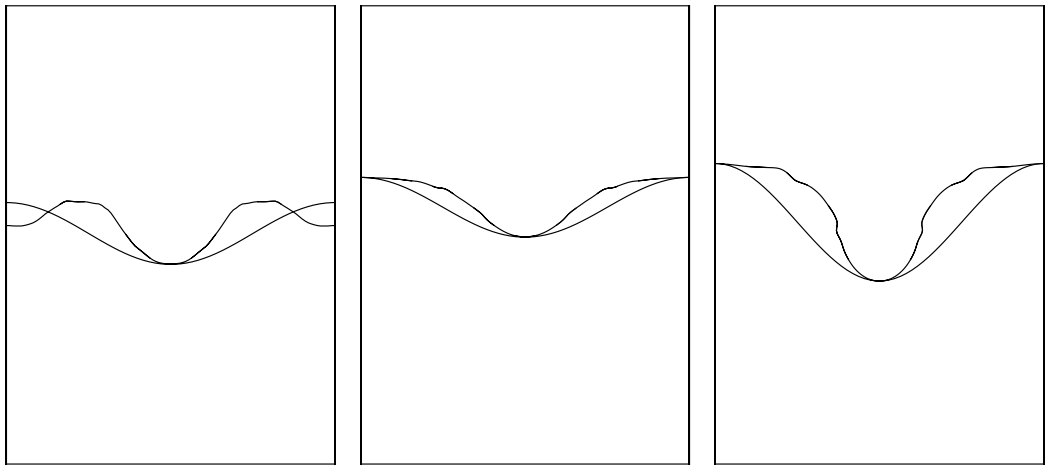

Figure 7.8: A test of the sine-shaped interface of the linear theory for the air-helium case. Sine waves of the same amplitude are superimposed on plots of the nonlinear interface: a) $t = 22\mu$s (the vertical scale in this frame has been stretched 15 times to show the details of the inversion process), b) $t = 90\mu$s, and c) $t = 190\mu$s.

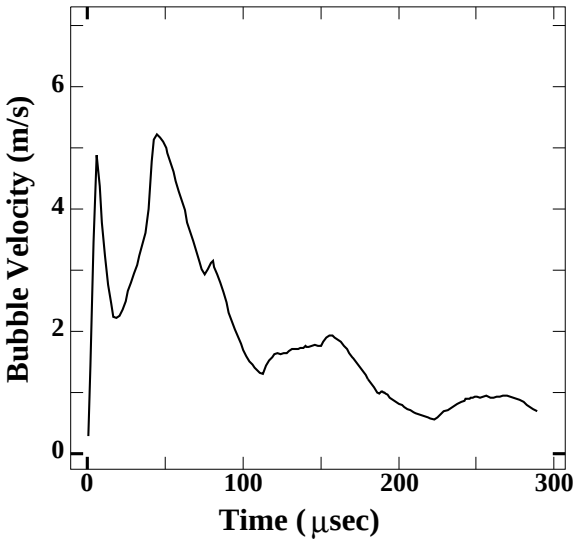

Figure 7.9: Air-helium simulation bubble velocity.

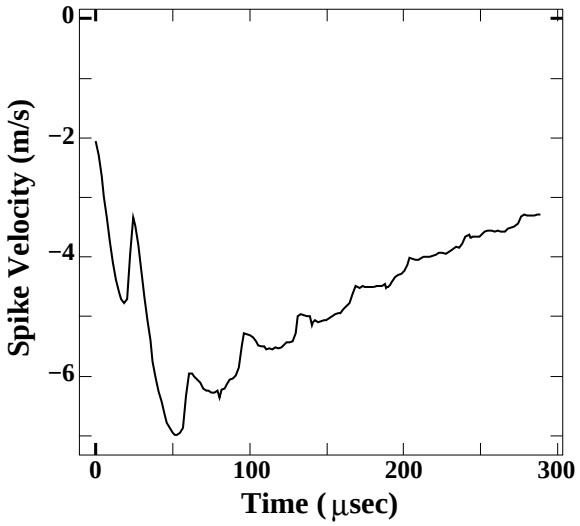

Figure 7.10: Air-helium simulation spike velocity.

with experiments. This dual agreement is possible due to the effects of the nonlinear, compressible waves and growth rate decay observed in the simulations. Thus even though the linear theory agrees with the nonlinear theory at early times it lacks the features that reduce the nonlinear simulation growth rate and, hence, fails to agree with experiment.

7.3 Potential Flow Model

The potential flow model of Hecht et al. [46] is intended to predict the bubble velocity in the Rayleigh-Taylor and Richtmyer-Meshkov instabilities for all times following shock refraction. For the Richtmyer-Meshkov instability it applies only to the case of a reflected shock wave and thus the following discussion applies only to the air-SF_6 simulations.

We have not made the detailed calculations necessary to find the potential

flow growth rates at early times and instead concentrate on the asymptotic velocity predicted by the model and confirmed in section 6.2. In that section we find that the predicted t^{-1} decay rate is nearly correct but that there is an offset between the potential flow model and the front tracking simulations. As the potential flow model is an incompressible model it cannot account for the early time compressible features which we find to be so important in the bubble dynamics (section 7.1). We believe, then, that model fails to agree completely because it is applied too early, before its assumptions are valid, and that the agreement would be better if the model was applied to the conditions later in the run when compressibility is less important. More work needs to be done to confirm this. However, this model does help to justify the decay in the growth rates.

7.4 Fraley's Model

Fraley's model (see section 2.1.3), like the potential flow model, applies only to the case of a reflected shock. Using his weak shock approximation we find his model predicts a growth rate of 9.31m/s for the air-SF_6 simulations. This compares well with the experimental value of 9.18m/s. This apparent agreement is, in the author's opinion, fortuitous. Since this model is based on a linearization of the Euler equations it has the same region of validity as the linear theory of Richtmyer and Yang et al. This model also makes a sinusoidal interface assumption. In addition, it predicts a single velocity which, given the decaying growth rates in the simulation, would give poor agreement had

the measurement period been different.

7.5 Improved Theories

It is interesting at this point to speculate on the possible forms of improved theories of the Richtmyer-Meshkov instability which correctly predict perturbation growth rates and amplitudes. An improved theory should have the following features:

1) Good agreement with experiments or simulations.

2) A range of validity incorporating multiple timescales

3) A minimum of simplifying assumptions

4) Ease of solution

Ideally, a successful model will allow useful simplifications or approximations which can be used to easily estimate growth rates in the same way that the impulsive model does. The discussion regarding growth rate decay in Chapter 6 suggests that simple scaling laws apply to the late time interface growth rate. A model which successfully predicts these laws will be especially useful.

Considering the relative success of the incompressible potential flow model it appears that is necessary to relax the linear and/or the sinusoidal interface assumptions. One approach is to allow multiple sinusoidal modes in the solution to the linearized equations. Indeed, the nonlinear pressure waves of Figures 7.2, 7.4 and 7.7 do have the appearance of second harmonics. This route is currently being attempted by Zhang [73].

Another possibility would be to extend the potential flow model to include

the spike regime. The current model assumes a free surface and the spike will be singular in nature, so to make the extension one must allow $A < 1$.

The development of an improved model of the Richtmyer-Meshkov instability will be a significant advance, for it should lead to an improved understanding of the important mechanisms in interface development.

Chapter 8

Validation and Measurement Sensitivity

In this chapter the front tracking simulations are validated and issues of diagnostic sensitivity are discussed.

8.1 Comparison to Linear Theory

The linear theory of Richtmyer [62] and Yang, et al. [71] described in Chapter 2 provides a unique method to validate the the early time behavior of the nonlinear front tracking simulations. The validation is accomplished by running the nonlinear simulations with very small amplitudes and comparing the results to the linear theory. Since the linear theory applies in the limit of small amplitudes the nonlinear simulations are expected to converge to the predictions of the linear theory as the amplitudes are reduced. It should be noted that in the linearization the amplitude growth rate $\dot{a}(t)$ is proportional to the initial amplitude $a(0-)$ and that the convergence is in the normalized growth rate $\dot{a}(t)/a(0-)$.

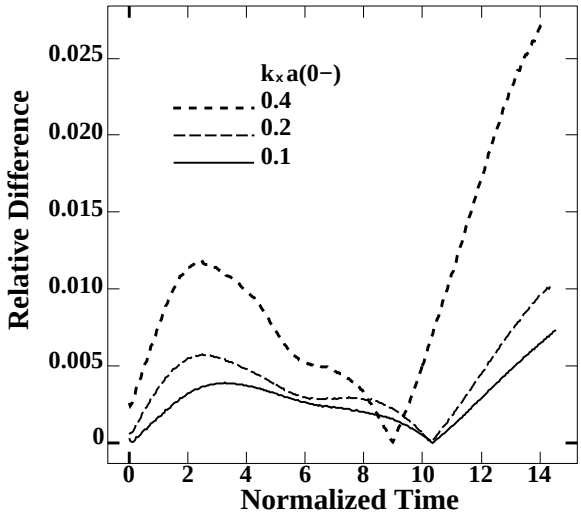

Figure 8.1: Convergence of the nonlinear air-SF_6 simulations to the linearized solution for small amplitudes. Amplitude convergence is measured in terms of the relative difference between the nonlinear and linear solutions, $|a(t) - a_{lin}(t)|/(|a_{lin}(t)| + |a(0-)|)$ where $a(0-)$ is the initial amplitude of the perturbation. The horizontal axis is in dimensionless time units kc_0M_0t, where k is the wave number of the perturbation, c_0 is the sound speed in the gas ahead of the incident shock and M_0 is the incident shock Mach number.

Figure 8.1 presents the convergence of nonlinear air-SF_6 simulations to the linear theory. The simulations use the experimental parameters of Table 4.1 except that they use a series of reduced initial amplitudes with $ka(0-) = 0.4$ (experimental value), 0.2 and 0.1. We can see from this figure that the nonlinear simulations are indeed converging to the results of the linear theory as the initial amplitude is reduced.

Figure 8.2 shows the results of a similar set of simulations for air-helium using the experimental gas parameters of Table 4.2 and, again, a series of reduced amplitudes with $ka(0-) = 0.2, 0.1$ and 0.05. The experimental value of $ka(0-)$ is 0.31. Once more we see convergence of the nonlinear simulations

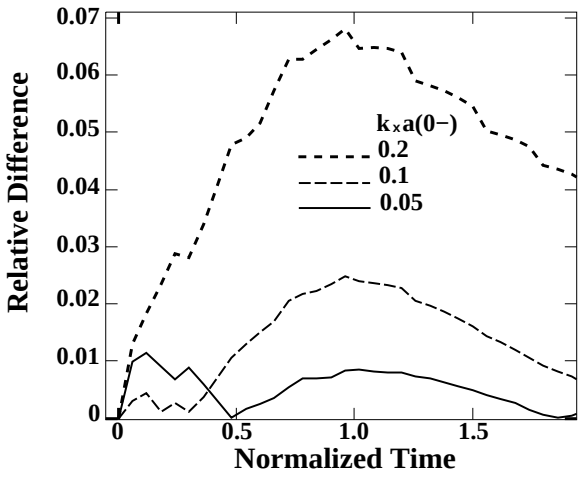

Figure 8.2: The convergence of the nonlinear air-helium simulations to the linearized solution for small initial amplitudes.

to the results of the linear theory at early times.

Based on the success of these tests we are confident that the code is correct and that the refraction process is computed correctly. It is a unique feature of the front tracking code that we can precisely measure the interface position and perform such diagnostics.

It is clear from Figure 8.2 that the convergence of the air-helium simulations is not as good as with air-SF_6. Since the convergence is in the limit of small amplitudes it is likely that we are not using amplitudes small enough to see good agreement.

Another point of agreement between the linear theory and the nonlinear simulations is in the amount of compression caused by the shock. This is seen in Figures 8.1 and 8.2 as a zero amplitude differential at $t = 0$. According to equation (2.5) the linear theory predicts a compression of the interface

perturbation to 83.2% of its original value. The nonlinear simulations agree well with this value, even at full experimental amplitudes where the simulations predict compression at a level of 83.7%. Compare this to the method used by Benjamin in [4] and [6] where he estimates the post-shock amplitude as the y-intercept of a least squares fit to the experimental data (see section 2.2.2).

One interesting aspect of the convergence of the nonlinear theory to the linear theory is that we do not see an appreciable increase in the time of agreement between the theories as we reduce the nonlinear amplitude. This is evident from Figure 8.3 which shows the convergence of the nonlinear air-SF_6 simulation growth rates to the linear theory growth rates in terms of $\dot{a}(t)/a(0-)$. The nonlinear simulations agree well with the linearized theory until they approach the growth rate peak at $t_* \approx 11$ (in normalized time units $t_* = Mckt$, M being the incident shock Mach number and c the ahead sound speed) when they begin to diverge from the linear theory. We see that the simulation growth rates approach those of the linear theory with reductions in amplitude, but without any real increase in the time of agreement. A similar phenomenon occurs in the air-helium simulations.

In addition, it has been widely assumed that there is an amplitude threshold below which the linear theory is valid. This is the case for the Rayleigh-Taylor instability [65]. As can be seen in Figure 8.4 there is no such threshhold for the Richtmyer-Meshkov instability since at the time of growth rate disagreement we have widely different amplitudes. Considering the discussion in Chapter 7 regarding the influence of shock curvature on the growth rate, it

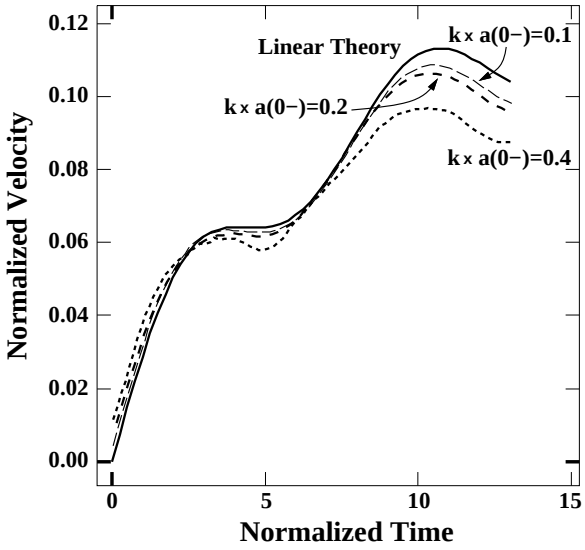

Figure 8.3: Normalized growth rates from air-SF_6 linear theory convergence tests.

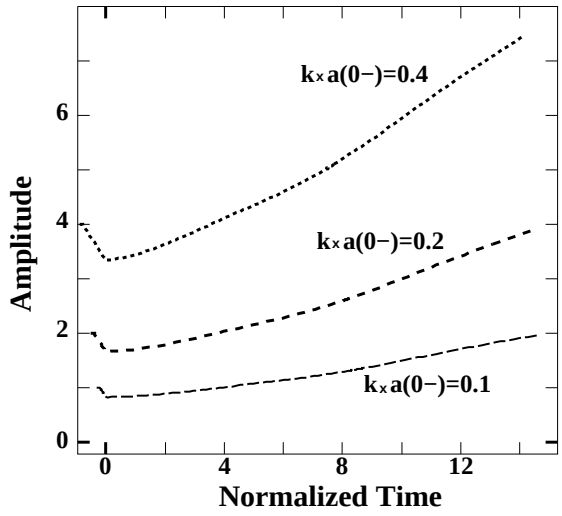

Figure 8.4: Amplitudes corresponding to the air-SF_6 growth rate convergence tests.

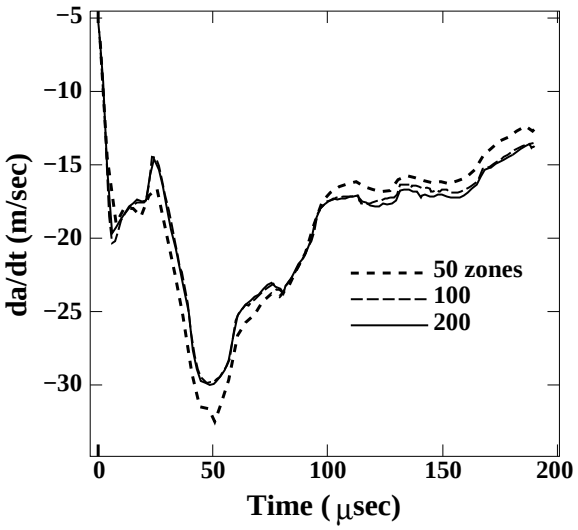

Figure 8.5: Perturbation amplitude growth under mesh refinement for the air-helium simulation. This plot shows the results of simulations using 50, 100 and 200 zones per wavelength. The growth has converged by 100 zones.

is possible that these effects decrease slowly with reductions in amplitude.

8.2 Mesh Refinement

Figure 8.5 shows a mesh refinement test for the air-helium simulations where resolutions of 50, 100 and 200 zones per wavelength are used. As can be seen from the figure, the growth rate has converged by 100 zones, the level used for the results presented in Chapter 4.

Figure 8.6 shows a similar test for the air-SF_6 simulations at resolutions of 62, 125 and 250 zones per wavelength. It appears from this figure that we do not have convergence in the growth rate. In fact, the differences in growth rates between 62 and 125 zones and 125 and 250 zones are nearly the same, which would indicate that we are very far from achieving convergence. A resolution

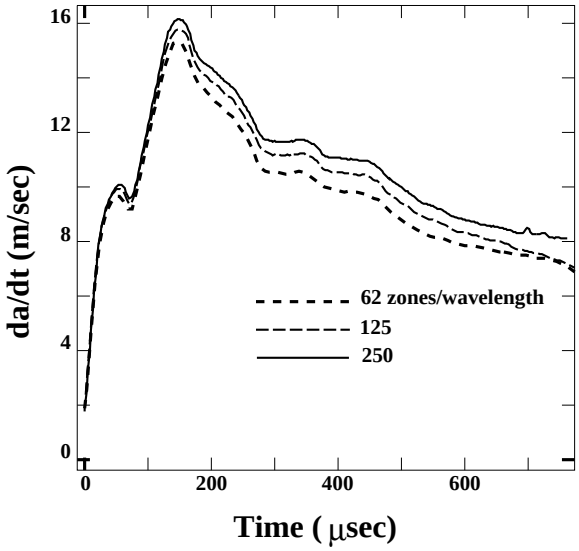

Figure 8.6: Mesh refinement studies for air-SF_6 at resolutions of 62, 125 and 250 zones per wavelength.

of 125 zones per wavelength, however, has been sufficient for convergence in other simulations of this type [6, 9, 29, 56] and the cause to this apparent lack of convergence is not likely to be underresolution.

In order to understand the convergence behavior of the growth rate we look at the bubble and spike behaviors separately. Referring to Figures 8.7 and 8.8 we see that there is relatively little change in the bubble velocity with mesh refinement and that most of the refinement changes take place in the region of the spike. Due to the smaller radius of curvature at the spike tip compared to the bubble tip and the larger amount of wave activity taking place in this region this region will be more sensitive to changes in the mesh.

We suspect that the convergence behavior is due to the extreme sensitivity of the pointwise amplitude measure to local oscillations in the interface am-

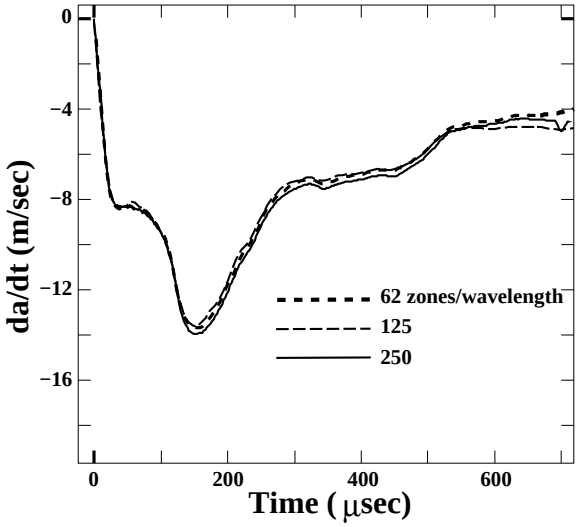

Figure 8.7: Mesh refinement tests for the air-SF_6 bubble velocities. The bubble velocity has converged.

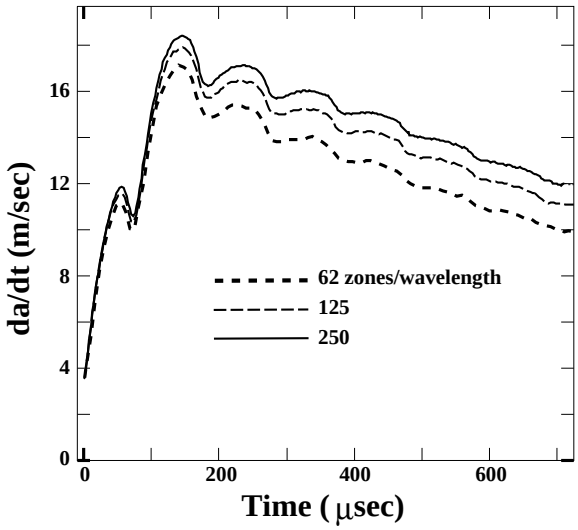

Figure 8.8: Mesh refinement tests for the air-SF_6 spike velocity. The spike velocity continues to increase with mesh refinement.

plitude. Indeed, convergence of the simulations to the correct weak solutions of the Euler equations would be expected to take place in L^1 or L^2 while the pointwise measure we are using is an L^∞ measure. Unfortunately, no L^1 consistent measure of interface amplitude is currently implemented and the cause of this convergence behavior remains unresolved.

We have found that the growth rates are also sensitive to the CFL constant used in the simulations. Again this behavior is localized to the spike tip and almost certainly has the same cause as the lack of convergence under mesh refinement.

Chapter 9

Future Work and Conclusion

9.1 Future Work

There is still much work to be done on the Richtmyer-Meshkov instability. There is as of yet no complete understanding of the important physical effects which control the instability.

Of particular importance is an understanding of the growth rate decay, for while this is not evident in the experiments of Benjamin or Meshkov, it is a very important feature of the simulations. The development of models which improve upon the linear theory, impulsive model and the potential flow model should help.

It will also be useful to study the effects of diffusion along the interface both before and after shocking. It is possible that diffusion is responsible for the difference between simulation and experimental amplitudes as well as the difference in translational velocities. New simulations and experiments are needed for this.

9.2 Conclusion

In this paper we have presented the results front tracking simulations of the experiments of Benjamin and Meshkov were presented. It was found that much of the interface behavior can only be explained in terms of nonlinear, compressible physics that is not captured in the simplified linear theory and impulsive model. We have shown that our simulations give better agreement with experimental growth rates than previous simulations and we discuss various reasons for the remaining differences. Finally, we discuss the asymptotic behavior of the interface velocities by examining simulations which deal with post- experimental time periods.

This paper presented the results of front tracking simulations of shock tube experiments by Benjamin and Meshkov. It was found that the perturbation growth rate predictions of these simulations are in much better agreement with those seen in experiment than has been found in previous simulations or theories. Simulations have previously predicted growth rates up to 200% larger than experiment which agrees with the theoretical predictions.

This improved agreement is explained in terms of the accuracy and stability of the front tracking method. Another reason for the improved agreement is that the growth rate measurements are made during the experimental time period. Errors in measurement timing can dramatically affect the apparent results.

A detailed analysis of the growth rate curve for the air-SF_6 simulations was made. This analysis showed that nonlinear and compressible effects are very

important in the history of the perturbation growth and cannot be ignored. Thus the assumptions of the theories, linearity and incompressibility, are violated in the experiments. The invalidity of these assumptions contributes to disagreement between the theories and experiment.

The long term development of the interface was considered. It was shown that the bubble velocities were nearly consistent with a potential flow model which predicts a decay like t^{-1}. In addition, it was shown that the spike velocities could also be fit by a power law.

Bibliography

[1] A. N. Aleshin, E. G. Gamalli, S. G. Zaitsev, E. V. Lazareva, I. G. Lebo, and V. B. Rozanov. Nonlinear and transistional stages in the onset of the Richtmyer-Meshkov instability. *Sov. Tech. Phys. Lett.*, 14:466–468, 1988.

[2] D. Arnett, B. Fryxell, and E. Muller. Instabilities and nonradial motion in SN 1987a. *Astrophysical J.*, 341:L63–L66, 1989.

[3] J. Bell, P. Colella, and J. Trangenstein. Higher order Godunov methods for general systems of hyperbolic conservation laws. *J. Comput. Phys.*, 82:362–397, 1989.

[4] R. Benjamin. Shock and reshock of an unstable fluid interface. In *Proceedings of Third International Workshop on The Physics of Compressible Turbulent Mixing at Royaumont France*, pages 325–332. 1991.

[5] R. Benjamin. Experimental observations of shock stability and shock induced turbulence. In W.P. Dannevik, A.C. Buckingham, and C.E. Leith, editors, *Advances in Compressible Turbulent Mixing*, pages 341–348. National Technical Information Service, U.S. Department of Commerce, 5285 Port Royal Rd. Springfield VA 22161, 1992.

[6] R. Benjamin, D. Besnard, and J. Haas. Shock and reshock of an unstable interface. LANL report LA-UR 92-1185, Los Alamos National Laboratory, 1993.

[7] I. B. Bernstein and D. L. Book. Rayleigh-Taylor instability of a self-similar spherical expansion. *Astrophysical Journal*, 225:633–640, 1978.

[8] D. Besnard, C. Cavailler, L. Dagens, P. Figeac, M. de Gliniasty, J.F. Haas, P.A. Holstein, J. Montigny, C. Parisot, V. Rupert, B. Sitt, and N. Wilke, editors. *Procedings of Third International Workshop on the Physics of Compressible Turbulent Mixing at Royaumont, France*. CEA, 1991.

[9] D. Besnard, J. Glimm, J.F. Haas, R.M. Rauenzahn, V. Rupert, and D. Youngs. Numerical simulation of 2d shock-tube multimaterial flow. In *Proceedings of Third International Workshop on The Physics of Compressible Turbulent Mixing at Royaumont France*. 1991.

[10] P. J. Blewett. Private communication, 1993.

[11] R. Bonazza. *X-Ray Measurements of shock-induced mixing at an air/xenon interface*. PhD thesis, California Institute of Technology, 1992.

[12] D. L. Book. Acoustic amplification in imploding spherical shells. *Phys. Rev. Letters*, 41(22):1552–1555, 1978.

[13] D. L. Book. Convective instability of self-similar spherical expansion into a vacuum. *J. Fluid Mech.*, 95(4):779–786, 1979.

[14] D. L. Book and I. B. Bernstein. Soluble model for the analysis of stability in an imploding compressible liner. *Phys. Fluids*, 22(1):79–88, 1979.

[15] D. L. Book and I. B. Bernstein. Fluid instabilities of a uniformly imploding ablatively driven shell. *J. Plasma Physics*, 23(3):521–533, 1980.

[16] B. Boston, J. Glimm, J. W. Grove, R. Holmes, and Q. Zhang. Multiscale structure for hyperbolic waves. Report No. SUNYSB-AMS-93-18, State Univ. of New York at Stony Brook, 1993. Proceedings of the International Conference on Nonlinear Evolution Partial Differential Equations, Beijing, P.R. China 1993.

[17] B. Boston, J. W. Grove, L. F. Henderson, R. Holmes, D. H. Sharp, Y. Yang, and Q. Zhang. Shock induced surface instabilities and nonlinear wave interactions. Report No. SUNYSB-AMS-93-20, State Univ. of New York at Stony Brook, 1993. Proceedings of Eleventh Army Conference on Applied Mathematics and Computing.

[18] B. Boston, J. W. Grove, and R. Holmes. Front tracking simulations of shock refractions and shock induced mixing. Report No. SUNYSB-AMS-93-19, State Univ. of New York at Stony Brook, 1993. Proceedings of the 19th International Symposium on Shock Waves.

[19] Brian Boston, John W. Grove, and Richard L. Holmes. Shock induced surface instabilities and nonlinear wave interactions. In *Matemática Contemporânea*, 1994. To Appear.

[20] R. Brouilette. *Rayleigh-Taylor instability in compressible fluids*. PhD thesis, California Institute of Technology, 1989.

[21] M. Brouillette and B. Sturtevant. Richtmyer-Meshkov instability at a continuous interface. In Y. W. Kim, editor, *Current Topics in Shock Waves: 17th International symposium on shock waves and shock tubes*, pages 284–289. AIP, 1990.

[22] J. Budzinski. *Planar Rayleigh Scattering Measurements of Shock Enhanced Mixing*. PhD thesis, California Institute of Technology, 1992.

[23] J. M. Budzinski, R. F. Benjamin, and J. W. Jacobs. Influence of initial conditions on the flow patterns of a shock-accelerated thin fluid layer. In *Physics of Fluid Letters (submitted)*, 1994.

[24] B. Bukiet, C. L. Gardner, J. Glimm, J. Grove, J. Jones, O. McBryan, R. Menikoff, and D. H. Sharp. Applications of front tracking to combustion, surface instabilities and two-dimensional Riemann problems. In *Transactions of the Third Army Conference on Applied Mathematics and Computing, ARO Report No. 86–1*, pages 223–243, 1986.

[25] D. E. Burton and A. K. Harrison. Numerical simulation of 2d shock-tube multimaterial flow. In *Proceedings of Third International Workshop on The Physics of Compressible Turbulent Mixing at Royaumont France*, pages 345–356. 1991.

[26] S. Chandrasekhar. *Hydrodynamic and Hydromagnetic Stability.* Dover Publications, New York, 1981 (original Oxford edition 1961).

[27] Y. Chen, J. Glimm, D. H. Sharp, and Q. Zhang. A comparative statistical analysis of a two phase flow mixing problem. In *In preparation.*

[28] I-L. Chern, J. Glimm, O. McBryan, B. Plohr, and S. Yaniv. Front tracking for gas dynamics. *J. Comput. Phys.*, 62:83–110, 1986.

[29] L. D. Cloutman and M. F. Wehner. Numerical simulation of Richtmyer-Meshkov instabilities. *Phys. Fluids A*, 4:1821–1830, 1992.

[30] P. Colella. A direct Eulerian MUSCL scheme for gas dynamics. *SIAM Journal on Computing*, 6:104, 1985.

[31] P. Colella and P. Woodward. The piecewise parabolic method (PPM) for gas-dynamical simulation. *J. Comput. Phys.*, 54:174, 1984.

[32] R. Courant and K. Friedrichs. *Supersonic Flow and Shock Waves.* Springer-Verlag, New York, 1976.

[33] W.P. Dannevik, A.C. Buckingham, and C.E. Leith, editors. *Advances in Compressible Turbulent Mixing.* National Technical Information Service, U.S. Department of Commerce, 5285 Port Royal Rd. Springfield VA 22161, 1992.

[34] P. Daripa, J. Glimm, J. Grove, W. B. Lindquist, and O. McBryan. Reservoir simulation by the method of front tracking. In *Proc. of IFE/SSI seminar on Reservoir Description and Simulation with Emphasis on EOR*, Oslo, September 1986. Institute for Energy Technology and Scientific Software-Intercomp.

[35] G. Dimonte and B. Remington. Richtmyer-Meshkov experiments on the nova laser at high compression. *Phys. Rev. Lett.*, 70(12):1806–1809, 1993.

[36] G. Fraley. Rayleigh-Taylor stability for a normal shock wave-density discontinuity interaction. *Phys. Fluids*, 29(2):376–386, 1986.

[37] B. Fryxell, E. Muller, and D. Arnett. Instability and clumping in SN 1987a. I. early evolution in two dimensions. *The Astrophysical Journal*, 367:619–634, 1991.

[38] J. Glimm, J.W. Grove, Y. Chen, and X.L. Li. Chaotic mixing at unstable interfaces. In *3rd International Workshop on the Physics of Compressible Turbulent Mixing*, pages 19–28. CEA DAM, 1991.

[39] J. Glimm, X. L. Li, R. Menikoff, D. H. Sharp, and Q. Zhang. A numerical study of bubble interactions in Rayleigh-Taylor instability for compressible fluids. *Phys. Fluids A*, 2(11):2046–2054, 1990.

[40] J. Glimm, W. B. Lindquist, and Q. Zhang. *Front Tracking, Oil Reservoirs, Engineering Problems and Mass Conservation*, volume 29 of *IMA Volumes in Mathematics and its Applications*. Springer-Verlag, New York–Heidelberg–Berlin, 1991.

[41] J. Goodman. Convective instability of hollow sedov-Taylor blast waves. *Astrophysical Journal*, 358:214–228, 1990.

[42] A. R. Gourlay. Splitting methods for time dependent partial differential equations. In D. Jacobs, editor, *The state of the art in numerical analysis, proceedings of the conference on the state of the art in numerical analysis*, pages 757–796. 1976.

[43] J. Grove, R. Holmes, D. H. Sharp, Y. Yang, and Q. Zhang. Quantitative theory of Richtmyer-Meshkov instability. *Phys. Rev. Lett.*, 71(21):3473–3476, November 1993.

[44] J. W. Grove. Applications of front tracking to the simulation of shock refractions and unstable mixing. *J. Appl. Num. Math.*, 14:213–237, 1994.

[45] J. W. Grove, Y. Yang, Q. Zhang, D. H. Sharp, J. Glimm, B. Boston, and R. Holmes. The application of front tracking to the simulation of shock refractions and shock accelerated interface mixing. In *Proceedings of the 4th International Workshop on the Physics of Compressible Turbulent Mixing, Cambridge University, Cambridge England*. State Univ. of New York at Stony Brook, 1993. Report No. SUNYSB-AMS-93-21, to appear.

[46] J. Hecht, U. Alon, D. Mukamel, and D. Shvarts. Simple potential flow models of Rayleigh-Taylor and Richtmyer-Meshkov bubble fronts. Technical Report Preprint, 1994.

[47] R. L. Holmes, J. W. Grove, and D. H. Sharp. Numerical investigation of Richtmyer-Meshkov instability using front tracking. In *Preprint*, 1994.

[48] J. W. Jacobs. The dynamics of shock accelerated light and heavy gas cylinders. *Phys. Fluids A*, 5(9):2239–2247, 1993.

[49] J. W. Jacobs, D. L. Klein, D. G. Jenkins, and R. F. Benjamin. Instability growth patterns of a shock-accelerated thin fluid layer. *Phys. Rev. Lett.*, 70(5):583–586, 1993.

[50] P. F. Linden, D. L. Youngs, and S. B. Dalziel, editors. *Proceedings of the 4th International Workshop on the Physics of compressible turbulent mixing.* Cambridge University Press, Cambridge, England, 1993.

[51] D. L. Lindl, R. L. McCrory, and E. M. Campbell. Progress toward ignition and burn propagation in inertial confinement fusion. *Physics Today*, 45(9):32–40, September 1992.

[52] D. Marcus, E. Puckett, J. Bell, and J. Saltzman. Numerical simulation of accelerated interfaces. In *Proceedings of Third International Workshop on The Physics of Compressible Turbulent Mixing at Royaumont France.* 1991.

[53] R. Menikoff. Errors when shock waves interact due to numerical shock width. LANL report LA-UR-93-1899, 1993.

[54] E. E. Meshkov. Instability of a shock wave accelerated interface between two gases. *NASA Tech. Trans.*, F-13:074, 1970.

[55] E. E. Meshkov. Instability of shock-accelerated interface between two media. In W.P. Dannevik, A.C. Buckingham, and C.E. Leith, editors, *Advances in Compressible Turbulent Mixing*, pages 473–503. National Technical Information Service, U.S. Department of Commerce, 5285 Port Royal Rd. Springfield VA 22161, 1992.

[56] K. A. Meyer and P. J. Blewett. Numerical investigation of the stability of a shock-accelerated interface between two fluids. *Phys. Fluids*, 15:753–759, 1972.

[57] K. Mikaelian. Rayleigh-Taylor and Richtmyer-Meshkov instabilities in multilayer fluids with surface tension. *Phys Rev A*, 42:7211, 1990.

[58] K. O. Mikaelian. Growth rate of the Richtmyer-Meshkov instability at shocked interfaces. *Phys. Rev. Lett.*, 71(18):2903–2906, 1993.

[59] E. Muller, B. Fryxell, and D. Arnett. Instability and clumping in SN 1987a. *Astron. Astrophys.*, 251:505–514, 1991.

[60] W. Noh and P. Woodward. SLIC (simple line interface calculation). In *Lecture Notes in Physics*, volume 59. Springer Verlag, New York, 1976.

[61] T. Pham and D. Meiron. A numerical study of Richtmyer-Meshkov instability in continuously stratified fluids. In *Proceedings of Third International Workshop on The Physics of Compressible Turbulent Mixing at Royaumont France*, pages 145–153. 1991.

[62] R. D. Richtmyer. Taylor instability in shock acceleration of compressible fluids. *Comm. Pure Appl. Math*, 13:297–319, 1960.

[63] V. Rupert. Shock-interface interaction: current research on the Richtmyer-Meshkov problem. In K. Takayama, editor, *Shock Waves, proceedings of the 18th international symposium on shocks waves*. Springer-Verlag, New York, 1992.

[64] R. Samtaney. Private communication, 1993.

[65] D. H. Sharp. An overview of Rayleigh-Taylor instability. *Physica D*, 12:3–18, 1984.

[66] G. Strang. On the construction and comparison of difference schemes. *SIAM J. Num. Anal.*, 5(3):506–517, 1968.

[67] B. Sturtevant. Rayleigh-Taylor instability in compressible fluids. In Hans Gronig, editor, *Proceedings of the 16th International Symposium on Shock Tubes and Shock Waves, Aachen W. Germany July 26-32, 1987*, page VCH, 1988.

[68] H. Takabe, M. Yamanaka, K. Mima, C. Yamanaka, H. Azechi, N. Miyanaga, M. Nakatsuka, T. Jitsuno, T. Norimatsu, M. Takagi, H. Nishimura, M. Nakai, T. Yabe, T. Sasaki, K. Yoshida, K. Nishihara, Y. Kato, Y. Izawa, T. Yamanaka, and S. Nakai. *Physics of Fluids*, 31:2884, 1988.

[69] B. van Leer. Towards the ultimate conservative difference scheme V. a second order sequel to Godunov's method. *J. Comput. Phys.*, 32:101–136, 1979.

[70] F. Wang, J. Glimm, J. Grove, B. Plohr, and D. Sharp. A conservative Eulerian numerical scheme for elasto-plasticity and application to plate impact problems. *Impact Comput. Sci. Engrg.*, 5:285–308, 1993.

[71] Y. Yang, Q. Zhang, and D. H. Sharp. Small amplitude theory of Richtmyer-Meshkov instability. In *Physics of Fluids A*, 1994. To Appear.

[72] S. Zaytsev, A. Aleshin, E. Lazareva, S. Titov, E. Chebotareva, V. Rozanov, I. Lebo, and V. Demchenko. Experimental investigation of Rayleigh-Taylor and Richtmyer-Meshkov instabilities. In *Proceedings of Third International Workshop on The Physics of Compressible Turbulent Mixing at Royaumont France*, pages 57–62. 1991.

[73] Q. Zhang. Private communication, 1994.